Crystallographic Texture and Microstructural changes in fusion welds of recrystallized Zry-4 rolled plates.

A Moya Riffo[a], M.A. Vicente Alvarez[a], J.R. Santisteban[a], P. Vizcaino[b], S. Limandri[c], M. R. Daymond[d], D. Kerr[d], J. Okasinski[e], J. Almer[e], S.C. Vogel[f]

[a] Neutron Physics Department, Centro Atómico Bariloche, CNEA-CONICET, Argentina

[b] Zirconium Technology Department, Centro Atómico Ezeiza, CNEA-CONICET, Argentina

[c] Facultad de Matemática, Astronomía y Física, Universidad Nacional de Córdoba, Argentina

[d] Dept. Mechanical and Materials Engineering, Queen's University, Kingston, Ontario, Canada

[e] Advanced Photon Source, Argonne National Laboratory, Argonne, USA

[f] Los Alamos Neutron Science Center, Los Alamos National Laboratory, Los Alamos, New Mexico, USA

Keywords: Zirconium; phase transformations; variant selection; texture; high energy X-Ray diffraction; fusion welding; heat affected zone; GTAW; PAW.

Abstract:

This work presents a detailed characterization of the microstructural and crystallographic texture changes observed in the transition region in a weld between two Zircaloy-4 cold rolled and recrystallized plates. The microstructural study was performed by optical microscopy under polarized light and scanning electron microscopy (SEM). Texture changes were characterized at different lengthscales: in the micrometric size, orientation imaging maps (OIM) were constructed by electron backscatter diffraction (EBSD), in the millimetre scale, high energy XRD experiments were done at the Advanced Photon Source (USA) and compared to neutron diffraction texture determinations performed in the HIPPO instrument at Los Alamos National Laboratory .

In the heat affected zone (HAZ) we observed the development of Widmanstätten microstructures, typical of the α(*hcp*) to β(*bcc*) phase transformation. Associated with these changes a rotation of the *c*-poles is found in the HAZ and fusion zone. While the base material shows the typical texture of a cold rolled plate, with their *c*-poles pointing 35° apart from the normal direction of the plate in the normal-transversal line, in the HAZ, *c*-poles align along the transversal direction of the plate and then re-orient along different directions, all of these changes occurring within a lengthscale in the order of mm. The evolution of texture in this narrow region was captured by both OIM and XRD, and is consistent with previous measurements done by Neutron Diffraction in the HIPPO diffractometer at Los Alamos National Laboratory, USA.

The microstructural and texture changes along the HAZ were interpreted as arising due to the effect of differences in the cooling rate and β grain size on the progress of the different α variants during transformation. Fast cooling rates and large β grains are associated to weak variant selection during the β–>α transformation, while slow cooling rates and fine β grains result in strong variant selection.

1. Introduction

Zirconium alloys are widely used in the nuclear industry for the construction of pressure tubes, vessels or fuel cladding. The fabrication route of some of these components involves welding of plates, rods or tubes. The welding process produces important changes in the microstructure and crystallographic texture of the original material, especially in the heat-affected and fusion zones; this can impair mechanical properties, corrosion resistance and susceptibility to hydrogen failure. In particular, there is a strong correlation between the morphology of hydrides formed in service and the stress and crystallographic texture of the α-Zr matrix. Changes in the crystallographic texture due to the welding process may leave the material susceptible to hydride cracking, due to the formation of harmful hydride morphologies in the heat affected zone. A deep characterization of the effect of weld in the crystallographic texture is needed to have a better control on the effect of the welding method on the piece performance.

At high temperatures, pure zirconium undergoes an allotropic phase transformation from an hcp (α) to a body-centred cubic (β) structure; the details of this temperature are dependent on the chemical composition of the alloy. The most popular zirconium alloys (Zircaloy-2 and Zircaloy-4) include Fe, Cr and Sn, and Oxygen as an interstitial element (~1000 – 1400ppm). While pure Zr undergoes an α–>β transformation at ~863ºC, the presence of the alloying elements generate an α+β region. In particular, O and Sn stabilise the α phase, while iron and chromium maintain the β phase stable at temperatures lower than for pure zirconium. For commercial Zircaloy-4, the α–>β starting temperature is around 810ºC while the full β transus is at approximately ~1020ºC. The particular dependence of these critical temperatures on the Cr, Sn and O content has been studied so far [1].

During fusion welding, as the Gas Tungsten Arc Welding (GTAW) and Plasma Arc Welding (PAW), the heat delivered produces melting of the material, and its subsequent solidification in a very thin region across the welding line (commonly known as the melting pool or fusion zone). Next to this region, the material is heated up to temperature below the solid to liquid limit, but high enough to produce important microstructural changes due to processes including solid to solid transformation or/and grain growth (heat affected zone or HAZ). In Zircaloy-4 welding, the region of the HAZ closer to the fusion zone may undergo a full β transformation (Tmax>1020ºC), while farther away the material may only have transformed partially to β (1020ºC >Tmax>810ºC). Finally, far enough from the welding line only grain growth in the α phase region may occur (Tmax<810ºC).

The α–>β–>α transformation has profound effects on the final microstructure of the material. In Zr and Ti alloys, during heating α grains transform to β grains which may experience grain growth at sufficiently high temperatures. During cooling at moderate and slow cooling rates, α phase precipitates in the form of plates maintaining a strict orientation relation and habit plane with the β matrix. A considerable amount of attention has been paid to the mechanism of formation of plate-shaped precipitates of the product phase where the transformation takes place through a thermally activated diffusional process. Three types of morphologies are commonly found: (i) α grains that precipitate as grain boundary allotriomorphs (GBA), which are plates forming along the high angle grain boundaries of the parent β phase, showing a precise orientation relationship between the α-plate and one of the β-grains sharing the boundary; (ii) Widmanstätten side plates nucleating at grain boundaries (primary side plates) or by branching out from GBAs (secondary side plates), growing in group resulting in the formation of a colony of parallel α-plates; and finally (iii) intragranular plates, which nucleate in the interior of the β-grains and give rise to the "basket weave" morphology. All these plates also obey fairly strict orientation relations with the parent β grain.

In our case of fusion welds of Zircaloy-4, α grains changed from an equiaxed shape (typical of recrystallized materials) to acicular or Widmanstätten grains after the α–>β–>α transformation. Previous works showed that the parallel plate and the “basket weave” morphology are most commonly found in these welds, probably due to the cooling rates involved during GTAW and plasma welding [2].

Besides microstructural changes, an aspect less commonly studied is related to the changes in the crystallographic texture that may occur across the weld, principally associated to this solid-solid phase transformation. As far as we know, the first determination of crystallographic texture in the HAZ was done in welds of Zr-2.5Nb hot rolled plates annealed at high temperature [3;4]. Although the texture of the hot rolled plate is different to that of cold rolled or recrystallized plate, the effect of welding is remarkable, giving rise to drastic changes of texture inside the HAZ. The texture after transformation shows *c* poles along the RD (welding direction) and *c*-poles close to the ND of the plate, not observed in the original material. Welds of two Zircaloy-4 plates were studied by TOF neutron diffraction technique in Ref [5]. The aim of that work was to characterize the residual stress profile across the weld. The strong variations of peak intensity as a function of the position in the HAZ hindered the use of a unique diffraction peak to state the strain profile but also indicated important texture changes. Determination of the texture in the HAZ was done by neutron diffraction due to the large grain size of the α colonies. It was shown that the typical cold rolled texture of the base material changes to a more randomly oriented texture inside the HAZ. In more recent papers [6,7,8], it was revealed that texture also evolves inside the HAZ. In Ref [6] the texture along a GTAW weld of two cold rolled Zircaloy-4 plates was determined by TOF neutron diffraction in HIPPO at LAN. Two coupons were extracted at different locations inside the HAZ. Close to the fusion zone, the texture is similar to that reported in Ref [5] showing a more random distribution of orientations, however close to the base material, still inside the HAZ, the material develops a sharp texture with an intense *c* pole aligned to the TD of the plate. In Refs [7and 8], texture changes were studied by EBSD in resistance welded cold worked stress relieved Zircaloy-4 plates and laser-welded Zircaloy-2 tubes, respectively. Although the measured pole figures had low statistics due to the large size of the α colonies, texture variations inside the HAZ could be clearly observed.

The evolution of texture during the α–>β–>α transition in both Zr and Ti alloys has been a subject of attention of the scientific community during the last decade. A series of papers were devoted to describe these changes, including in-situ [9, 10,11, 12, 13,14] and ex-situ texture measurements [15,16,17, 18, 19]. From the beginning, it is clear that the effect of the transformation on texture is ruled by the Burgers’ crystal relation between the α and β phases [20]. In-situ diffraction experiments in high energy X-Ray sources or neutron sources give the possibility to access the texture of the α phase at high temperatures before transformation, of the α and β phases in the α+β region, the evolution of the β phase at high temperature and the inherited α texture after cooling. This new evidence puts some light on the importance of variant selection (i.e. not all possible variants are equally likely) during heating and cooling and during β grain growth. However, it is still not clear which is the mechanism operating during variant selection, and/or the effect of the initial texture and microstructure and/or the effect of the thermal cycle parameters (maximum temperature, heating and cooling rates) on the final texture.

This work aims to characterize in detail the changes of microstructure and texture of two fusion welds (GTAW and PAW) of Zircaloy-4 cold rolled and recrystallized plates and to understand the origin of these changes. Different techniques were used to characterize the microstructure (optical and scanning electron microscopy with electron backscatter diffraction). The evolution of texture within the HAZ was measured by high energy X-Ray diffraction methods (HE-XRD) in transmission geometry in cylindrical samples (3mm diameter) extracted from the weld. Sample rotation permits us to have access to complete experimental pole figures of several diffraction peaks. The use of this setup provides sound data even in the case of large α grain colonies with a spatial resolution of the order of ~mm. The results of this experiment were complemented with analysis based on the EBSD maps and also compared to neutron diffraction texture determinations. The paper is organized in the following way: in the next section the sample and experimental setup is presented; in section 3 we present the results, describing the evolution of the microstructure and texture across the weld. In section 4 we make use of texture simulations to interpret the results obtained in the XRD experiments. In section 5 we analyze the different textures observed in the welds in terms of the existing knowledge on the effect of the α–>β–>α transformation on the final texture. Finally, in section 6 we summarize the main conclusions.

2. Experimental

2.1. Sample preparation

The material used in this work is a cold rolled and recrystallized plate of Zircaloy-4 (ASTM B352, grade R60804) manufactured by WAH-CHANG, USA. The plate thickness is 6mm and was provided by

INVAP SE in Argentina. This material is part of that used to build the reflector vessel of the experimental reactor OPAL (ANSTO, Australia, [21]). During annealing after cold rolling, complete recrystallization occurs and the microstructure ends with a dislocation free equiaxed grain structure of 10-20µm size.

Two plates of 10cmx50cmx0.6cm size were welded along the rolling direction following two different welding methods: gas tungsten arc welding (GTAW) and plasma arc welding (PAW). In the case of GTAW, a Zircaloy-4 filler rod was used during welding. For the PAW the power delivered was estimated to be ~1830 J/s and a welding speed of 3.83 mm/s; and for GTAW the power delivered was ~2300 J/s and the welding speed 2.94 mm/s.

Figure 1 shows a schematic drawing of the weld, with the weld bead along the rolling direction. To perform the microstructural and diffraction characterization, transverse specimens of 20mm length were cut, as indicated by the dashed green lines in Figure 1. Cylinders of 3mm diameter were machined from these test specimens to perform the high energy X-Ray diffraction experiment with the axial direction of the cylinders along the transverse direction of the plate. These samples were also charged with H to study the effect of different microstructures on the distribution and state of hydrides (in a separate work). Microstructure characterization was done with optical microscopy under polarized light and scanning electron microscopy (SEM) with electron backscatter diffraction (EBSD). The metallographic preparation of the samples involved mechanical polishing, chemical etching using a solution of nitric acid (47 %), distilled water (50 %) and hydrofluoric acid (~ 3 %) and a final anodizing procedure [22] to reveal the microstructure under polarized light. EBSD measurements were carried out in a scanning electron microscope FE-SEM Sigma- Carl Zeiss with a Schottky electron gun. The electron backscatter detector is an Oxford Nordlys Nano with a CCD camera with 1344×1024 pixels and a 40 mm × 35 mm front phosphor screen. The following SEM parameters were used for the acquisition: 20 keV incident energy, 120 µm aperture (corresponding to a specimen beam current of 1nA), 8.5 mm working distance, and 70º tilt angle. The step size was 2 µm and a 4×4 binning was set for the CCD camera. Dynamic background subtraction was performed for the Kikuchi patterns and a minimum of 7 bands were used to index each pattern. The acquisition software used was Flamenco.

2.2. High Energy X-Ray diffraction.

High-energy X-Ray diffraction (HE-XRD) experiments were performed at the 1-ID instrument of the Advance Photon Source, Argonne National Laboratory, USA. The experimental setup is in transmission geometry as shown in Figure 2(a), the X-Rays beam is monochromatic with an energy of 86keV (λ=0.144 Å), of 300x300μm size. The cylindrical sample was placed in a rotating holder with the rotation axis parallel to the axial direction of the cylinder. This rotation stage was placed in turn on a positioning table with x-y-z movement. A CCD detector was located behind the sample at a distance of ~1.8m. This 2D screen has a size of 20x20cm and is formed by a matrix of 2048x2048 pixels of 1μm size. More details about this experimental setup can be obtained elsewhere [23]. The X-Ray beam goes through the entire thickness of the sample, and the Debye-Scherrer diffraction cones project on the screen forming an image that is collected by the CCD. An example of such an image is shown in Figure 2(a). Considering the size of the illuminated area and the cylinder diameter, the effective gauge volume was ~2.1 mm^3. The cylinder was rotated 180º with an angular step of 5º, for each rotation angle θ an image was recorded. After 180º rotation, both sample and rotating holder were vertically displaced 1mm and then rotated again. For each vertical position, a set of 36 images were collected. A total of seventeen different positions were explored going from the welding line to a region inside the base material. Data processing involved several steps that are explained in more detail in Ref [23]. These steps are summarized as follows: first, in order to obtain intensities that depend only on the sample and the diffraction geometry the raw CCD images are corrected by dark current, flat-field and spatial distortion. Then, after proper identification of the beam center of the Debye rings, the *x*-*y* geometry of the screen was transformed into a polar one (ρ, φ), and the images were divided into 36 polar sections of 10º width. The distance of the Debye ring to the image center ρ can be easily transformed into *d*-spacing by applying Bragg's law. From each φ section, an intensity *vs.* *d*-spacing diffractogram can be constructed after φ averaging. An example of such a diffractogram is presented in Figure 2(b), where peaks corresponding to the two main phases present in the sample (α-Zr and Zr hydride) are indicated with different colors. The Zr hydride peaks correspond to the cubic δ phase and are omitted in the following analysis. For each vertical position we have a set of 36 images for each θ step, divided into 36 different φ sections, giving a total of 1296 diffractograms. Each diffractogram has associated a particular direction of the scattering vector, expressed in the sample reference system. Thus, from the intensity of each diffraction peak a pole figure can be constructed. Examples of poles figures obtained for the base material for the α-Zr (0002) and (10-10) planes are presented in Figure 2(c). It is straightforward to show that rotation of the cylinder along θ implies pole figure rotation along the transverse direction (east of the pole figure), while φ scanning (along the Debye ring) projects as 2 elliptical lines in the pole figures. With this experimental setup, complete pole figures can be constructed for each diffraction ring. In this particular case, a total of 10 peaks of the α-Zr phase could be captured by the detector, so up to 10 complete pole figures can be constructed for each position across the weld. The large volume of experimental data imposes the use of automatic processing. A homemade program written in MATLAB language was used to fit the diffraction peaks with pseudo-Voigt functions [24] (after proper background subtraction) and to store the optimized variables that define the shape of the peak (intensity, d-spacing, FWHM and Gauss to Lorentzian shape). Crystallographic texture analysis was done using the MTEX toolkit [25], a free license package that works under MATLAB. With this software, orientation distribution functions (ODF) for α-Zr were evaluated from the experimental pole figures for different positions across the welds. In all the cases studied, the error involved in the calculation of the ODF was below 3% as given by the MTEX software.

3. Results

3.1. Microstructure

Figure 3 shows a panoramic micrograph under polarized light of the two welds. The dashed green line indicates the center of the welding line. In what follows, distances are referred to this imaginary line. The superimposed white squares show the positions of the points where the high energy X-Ray beam impacts on the sample. The size of the squares corresponds to the actual area illuminated by the X-Ray beam ($300x300\mu m^2$). As expected, the microstructure changes drastically due to the welding process associated principally with the transformation from the high temperature β phase to the low temperature α phase during cooling. The main difference between the plasma and GTAW weld is the heat delivered during the welding process, being much larger in the case of the GTAW welding. In this last case, the welding pool shows a chisel-like shape, and the heat affected zone is much larger, with a size of up to ~11.5mm from the weld center (compared to ~7.5mm in plasma welding). In both welds, two imaginary vertical lines show up dividing regions with different color contrast. In PAW these lines appear at ~6.3mm and at ~7.3mm, in GTAW at ~10mm and at ~11.5mm. Those lines closer to the welding pool (at ~6.3mm in PAW and at ~10mm in GTAW) are sharp and well defined, separating two zones with marked differences in color contrast. Those lines further away from the welding line are more diffuse.

Figure 4 shows in detail the different grain morphologies found in the different regions of the weld in the case of GTAW. At the welding pool (Figure 4(a)), the maximum temperature surpasses the β to liquid solvus, and the microstructure after cooling is mainly formed of Widmanstätten α grains with the "basket weave" morphology. Beside the fusion zone, we found a region where the α grains are of Widmanstätten type with morphologies varying from "basket weave" closer to the melting pool limit (from 3 to 5mm to the welding line, see Figure 4(b) and 4(c)) to parallel plate morphology closer to the base material (see Figure 4(d-e)). Some GBA grains are observed in Figures 4(c) located at the boundaries of prior β grains. In this region, there are no indications of untransformed α grains. Hence in this region the maximum temperature varied with position but stayed below the β to liquid temperature (~1850ºC) and above the α+β to β temperature (~1020ºC). This region extends up to the location of the sharp imaginary line at 10mm. In the micrograph at ~10 mm (see Figure 4(e)), we observed Widmanstätten grains forming plate colonies of ~50-80 μm size (left of the figure), α grains with a more equiaxed shape of ~15μm size with a parallel plate sub-structure together with α grains without sub-structure, either with equiaxed shape or irregular grain boundaries (see center and right part of Figure 4(e)). The larger Widmanstätten colonies observed at the left are associated to α grains transformed to β and then re-transformed to α by nucleation of more than one nucleus per β grain. Smaller α grains with internal sub-structure are associated to α grains transformed to β and re-transformed to α as a unique parallel plate colony. Finally, α grains without sub-structure are associated to non-transformed grains. The irregular shape of some of these non-transformed grains may be produced by the movement of α/β grain boundaries over the α phase while the material is in the α+β region of the phase diagram. The fraction of small α grains with parallel plate substructure diminishes as moving towards the base material, while the fraction of α grains without sub-structure steadily increases. This characteristic defines the region limited by the two imaginary lines mentioned in reference to Figure 3. In this interface region, that starts at ~9.8mm and extends up to location of the second imaginary line (~11.5mm), transformed α grains and non-transformed grains coexist, hence the maximum temperature must have been in the α+β part of the phase diagram (~810ºC < T_{max} <~1020ºC). The microstructure of the base material (Figure 4(f)) is characterized by equiaxed grains of 10 to 20μm size. Grain growth was found to occur close to the interface region. The region that extends from the welding pool (~3mm) up to the second imaginary line at ~11.5mm is called hereafter the heat affected zone (HAZ). In the HAZ we can clearly separate two zones, one from the welding pool up to the first imaginary line where full β transformation occurs, and a second region (the interface) that lay in between these two imaginary lines, where partial transformation happens.

While the presence of Widmanstätten grains is an indicator of the β–>α transformation [26], the morphology of these grains ("basket weave" or parallel plate) correlates with the dependence with position of the β grain size and cooling rate at the β–>α transformation temperature [26,27]. As previously described by Perez et al. [2] on a Zircaloy-4 GTAW weld sample, there is a close relationship between both cooling rate and β grain size with grain morphology after transformation. At slow cooling rates, α–plates precipitate as parallel plate colonies (either as primary or secondary side plates) at the β grain boundaries and growth filling the entire β grain. At high cooling rates, large undercooling promotes the formation of intragranular α plates in the interior of the β matrix giving rise to the "basket weave" morphology. In coarse β grains, α plates with the "basket weave" morphology are also formed at moderate cooling rates. In this last case, the time needed for the parallel plate colonies to fill the entire β grain is long enough, and intragranular nucleation also occurs. According to Ref [28], during welding cooling rate is high close to the welding line, and decreases as towards the base material. The appearance of the "basket weave" morphology, dominating the microstructure at the welding pool (as shown in Figure 4(a)), and the changes observed in the HAZ, where the grains morphology varies from "basket weave" close to the limit with the melting zone and parallel plate close to the limit with the base material, is consistent with the expected dependence of the cooling rate with position [28]. Similar results were observed by Romero et al in controlled temperature gradient experiments done in Zircaloy-2 plates [13].

The maximum temperature as a function of the distance to the welding line was estimated using

Adam's equation [28], where the heat delivered during welding and the material conductivity for Zry-4 was used. The result of such calculation is shown in Figure 5(a) for GTAW, together with the fraction of β phase estimated in the α+β region. This curve was measured by Forgeron et al. [29], for Zircaloy-4 by calorimetric techniques in equilibrium condition. According to this calculation, the extension of the intercritical region where α+β coexist must be of the order of 2mm. However, from the optical micrographs of Figures 3 and 4 it is clear that this region is a little narrower, of the order of 1.5 mm. To understand this difference, we must consider that the material is out of equilibrium during welding. In the region located 10 to 12mm from the welding line in GTAW, the dwell time at high temperature was so short, that there was no time enough for the α–>β transformation to progress as in a constant temperature test, even though the maximum temperature maintains above 813ºC.

Besides grain morphology, in the melting pool and HAZ there is a clear dependence of the colonies' size with the distance to the weld center. This dependence is shown as black dots in Figure 5(b) for GTAW. Colony size is larger at the weld center with values of the order of ~300μm and decreases continuously down to values of ~50μm at the limit between the HAZ and the base material. This length is related to the size of the prior β grains at the moment of the β–>α transformation, and its large variation within the welded region is an indicator of the marked grain growth of β grains due to the high temperature reached during welding. High cooling rates and coarse β grains at the weld center and adjacent regions favor the formation of α plates with the "basket-weave" morphology. The width of the plates that form either the "basket weave" or the parallel plate sub-structures, increases with the distance to the weld center, as shown by the red triangles in Figure 5(b). This width correlates to the cooling rate at the β–>α transformation temperature as observed in Ref [27,30]. In our cases, cooling rates where estimated using theoretical calculations of the Rosenthal's equation [28] for both weld samples. Close to the fusion zone, the cooling rate was ~400ºC/s and close to the interface with base material was ~100-150ºC/s.

3.2. Crystallographic texture

Experimental pole figures were constructed for up to 10 different α-Zr diffraction peaks at each position indicated by the white squares in Figure 3. This set of pole figures was used to evaluate the orientation distribution function (ODF) with the MTEX software and pole figures were then recalculated from these ODF´s. The texture index was also evaluated from the ODF´s. This quantity, which is an indicator of texture sharpness, varies with position as shown in Figure 3 for GTAW. The complex dependence with position, with a drop at the welding pool, will be discussed later in terms of the colony size, and number of texture variants on a prior β phase grain.

Figure 6 shows the recalculated pole figures of the (0001), (11-20) and (10-10) planes for selected positions across the weld for both welding methods. Close to the welding pool, and due to the large grains size of the colonies, it was necessary to average the images corresponding to two neighboring points to construct the pole figures. In these cases the label associated to each set of pole figures refers to two distances instead of only one. In Figure 6 we also included pole figures determined by neutron diffraction, presented in Ref [6]. These pole figures were measured on specimens of ~2x4x6 mm^3 wide extracted from these samples at three different positions. For GTAW these specimens were taken out, one at the base material and two at different locations within the HAZ. For plasma welding, one was cut from the base material, one from the HAZ and the third one from the fusion zone. The great penetration of neutrons compared to X-Rays makes these texture determinations more representative of the actual material texture and are used here as a reference, however the limited spatial resolution of the technique prevents a detailed study of the texture changes that occur in regions of the order of mm.

Important changes of the crystallographic texture occur due to the welding process. The texture at the base material is typical of cold rolled and recrystallized Zr, with grains having their *c*-axis rotated ~35º from the normal direction in the normal-transversal plane, and either their (10-10) and (11-20) plane normal pointing along the rolling direction [31,32,33]. Actually, this texture is a fiber-like texture, as shown in the 2D plot of the ODF of Figure 7(a). From this graph it is clear that these orientations lie along two fibers with Euler angles (using Bunge Rotation Convention) φ_1=0, and 180º (section not showed on figure) and Φ ~35º. These fibers correspond to rotations along the *c*-axis of the hexagons (φ_2 rotation), so for some values of

φ_2 either the (10-10) or the (11-20) plane normal align with the RD. The probability distribution along the fiber is not constant, it shows maximum values for φ_2=0 and 60º and minimum values for φ_2=30º. The first orientation (φ_2=0 and 60º) corresponds to crystals having their (10-10) plane normal along the RD and is labeled C1+. The one with φ_2=30º correspond to crystals having their (11-20) plane normal along the RD and is named C2+. Similar orientations, lying along the fiber with φ_1=180º are named C1- and C2-. In Figure 7(c) we show schematically hexagons oriented accordingly to this set of orientations in the sample reference system. The origin of these fibers starts at the cold rolling stage, where grain rotation during deformation yields a fiber texture with an intense C1 and low C2 component. During subsequent annealing, recrystallization occurs and texture is modified with an intensification of C2 at the expense of C1 orientations [34]. Bozzolo et al [35] showed that the relative intensity of these two texture components is highly dependent on the annealing time and temperature, and the active mechanisms is preferential grain growth of the C2 grains during recrystallization. In a recent paper, Zhu et al [36] called these C1s orientations the 'tilted' {0001}<10-10> and the C2s orientations the 'tilted' {0001}<11-20>. Considering the origin of these texture components, we prefer to call them: C1s the "deformation" (g_{DF}) and C2s the "recrystallization" (g_{RX}) components.

In both GTAW and PAW weld, see Figures 6(a) and (b), the crystallographic texture is identical to that of the base material in the interface region adjacent to the base material, and then changes abruptly when crossing the first imaginary line located at ~10mm in GTAW and at ~6.3mm in PAW. In GTAW, at ~9.75mm, the fiber-like texture, characteristic of the base material, is replaced by a texture dominated by a sole orientation, corresponding to hexagons with their *c*-axis along the TD and the (11-20) plane normal along the RD. This orientation is responsible for the maxima of intensity at the TD in the (0001) pole figure and at the RD in the (11-20) pole figure. In terms of the ODF this orientation correspond to Euler angles (φ_1=0, ϕ=90º , φ_2=30º) and is called C3 in Figure 7. This component corresponds to grains with their {10-10} plane normal along the ND and the <11-20> axis along the RD: {10-10}<11-20> orientation. Hexagons with the g_{RX} and C3 orientations have all of their {11-20} plane normals along the RD, as shown in Figure 7(c). These two orientations differ by a ~60º rotation about the RD. Another texture component appears in the HAZ. This component is responsible for the low intensity (0001) pole that shows up close to the RD (~25º apart of the

RD in the RD-ND line). This new orientation is labeled C4 and appears relatively often in the HAZ with weak intensity. Still inside the HAZ and moving towards the welding line, the texture continuously evolves; at 7.75mm position, both the g_{RX} and C3 orientations have similar probability of occurrence. From this point up to the welding line, there are only small changes of the crystallographic texture, mainly associated to smooth variations of the probability of occurrence of the g_{RX}, C3 and other weak orientations close to the RD (named C5). Figure 7(b) shows the ODF corresponding to the texture reported in the HAZ at 6.75 and 7.75 mm from the welding line, where both g_{RX} and C3 orientations appear as the main texture components, with the g_{RX} orientation showing a higher probability of occurrence. At the fusion region, the crystallographic texture is far from being isotropic, moreover it shows the same characteristic as the texture observed in the region of the HAZ next to it. Table 1 presents a summary of the main components involved in the description of the texture in the weld with their corresponding Euler angles. In figure 8(a) and 8(b) we present the evolution of the volume fraction of the different texture components as a function of the position for the two welds. These volume fractions were calculated from the ODFs considering the contribution of all orientations within a sphere of 15º radius centered at the ideal orientation position. In the base material, g_{DF} and g_{RX} accounts for about 20% of the material, being the fraction of the g_{DF} components slightly higher. On the other hand, components C3 and C4 have low probability of occurrence with volume fractions below 3%. At the interface between the HAZ and the base material, C3 abruptly increases at the expense of both g_{DF} and g_{RX}. Inside the HAZ moving towards the welding line, g_{RX} gets stronger, while g_{DF} weakens. At the interface between the HAZ and the welding pool, g_{RX} and C3 become the most prominent texture components, with volume fractions as high as 16% and 8%, respectively.

Kearns factors for the three main directions of the sample [37] were evaluated from the (0001) pole figures of Figure 6(a) and are plotted as a function of the distance to the welding line in Figure 8(c). Each color corresponds to a principal direction of the sample (ND, TD and RD). From its own construction, the sum of the three coefficients must be 1. In the base material, Kearns factor are constant, with the highest values along the ND (K_{ND}~0.6), and the lowest values along the RD (K_{RD}~0.1). This occurs due to the high concentration of (0001) poles along the TD-ND line with an almost complete absence of (0001) poles along the RD. In the interface region (at 10.75mm), Kearns factors are identical to those values of the base material.

are found inside the HAZ. This point correspond to the region where partially phase transformation ($\alpha+\beta$) occurs. In the region of the HAZ at ~9.75, the Kearns factor drastically change, the K_{ND} coefficient drop and the K_{TD} and K_{RD} coefficients rise. This reflects the drastic texture variation occurring in this region, where the texture is now dominated by the C3 component and a less important contribution of the C4 component. From 9.75 to 7.5mm there is a constant rise of K_{ND} and a soft drop of K_{TD}. This variation is associated to the continuous increase of the probability of g_{RX} at the expense of C3 as shown in Figure 8(b). Note that, in this region, grain shape also changes from the parallel-plate to the "basket weave" morphologies, with a plate thickness that is constantly diminishing as the welding line is approached, as can be seen from Figure 5(b). From the welding line up to 7mm distant, the Kearns factors stay constant. As mentioned above, texture only change smoothly in this region. Note that, although the Kearns factors are close to 1/3, texture is far from being isotropic in this region.

Figure 6(b) presents the evolution of texture in the case of PAW. The same characteristics found in GTAW welding repeats in this case. As the HAZ is narrower for this welding method, the evolution of texture with distance is more marked than in GTAW. In the HAZ adjacent to the interface region, texture changes drastically from the fiber-like texture, characteristic of the base material, to one dominated by the C3 component. At 5-6mm from the welding line, g_{RX} and C4 orientations show up but the texture is still ruled by C3. At 4-5mm, g_{RX}, C4 and C3 components appear with similar probability, finally at 3-4mm C2 orientation seems to be the most probable orientation, but C3 and C4 still have a significant probability of occurrence.

Compared to the neutron diffraction determinations, we observe an excellent agreement of the present pole figures in both GTAW and PAW. In GTAW, the evolution of the crystallographic texture across the weld could be captured by neutron diffraction experiments. However in PAW, part of these changes was not seen, in particular the texture found at the region of the HAZ adjacent to the interface region could not be observed by neutron diffraction due to the rapid changes over short distances.

3.3. EBSD study of the HAZ-base material interface

Considering that the HAZ is larger in the GTAW sample, EBSD images were made only in this case. A clear observation that emerges from the X-Ray pole figures was the rapid appearance of the C3 component near the interface region of the HAZ adjacent to the base material. In order to investigate this with finer spatial resolution, we performed EBSD orientation maps of this interface region. Results are presented in Figure 9(a), where individually measured points were grouped into grains with < 5º misorientation. The optical micrograph of this region is the one shown in Figure 4(e). It is worth to mention that the plate sub-structures of the small α grains are not clearly defined in the EBSD map as in the optical image of Figure 4(e) due to the spatial resolution–of the map. Grains corresponding to the three main texture components were painted with different colors: g_{DF} grains in blue, g_{RX} grains in red and C3 grains in green (with a deviation tolerance angle of 15º from the ideal orientations of Table 1). The angle distribution of the grain boundary misorientations and texture were analyzed in different regions along this interface.

Three sections of 100μm width with different characteristics were defined and labelled as A, B and C.

Region C has all the characteristics observed in the base material, grains shows equiaxed shape with a size of ~10 to 15μm. The grain boundary misorientation function, shown in Figure8(c), displays a smooth dependence on misorientation angle over the full range with only a moderate maximum close to 30º. This misorientation distribution is similar to that of the base material, where recrystallized grains have no specific orientation correlation with their neighbors except for the effect of texture [35]. The crystallographic texture, here represented through the (0001) pole figure, is also typical of recrystallized cold rolled Zircaloy. In this region, g_{DF} and g_{RX} grains (blue and red, respectively) appear with higher frequency while only a few grains show the C3 orientation. It is interesting to note that according to the optical micrograph of Figure 4(e), an important fraction of α grains undergo the α–>β–>α transformation (those α grains with plate sub-structure). In spite of that, both the grain boundary misorientation function and the crystallographic texture show the same characteristics seen in the base material. This confirms at a smaller lengthscale the result presented in Figure 6(a), where the texture at 10.75, corresponding to the interface region, is identical to that of the base material. This behavior can be explain in terms of a texture memory effect, those grains that transform to β re-transform as α grains with the same orientation of the original α grain. A perfect memory effect has been reported by Romero et al. [13], where a strong variant selection occurs during cooling if the material is only partially transformed to β.

At the other end of the interface, in region A, the microstructure is characterized by Widmanstätten grains with the parallel plate morphology with a plate shape of ~50x10μm size. The grain boundary misorientation distribution now shows a prominent maximum at 60º, which is the characteristic misorientation of several colonies formed within the same β grain during the β–>α transformation [15]. The texture in this region is no longer dominated by the g_{DF} and g_{RX} grains, instead a more random (0001) pole figure is observed, with maxima out of the normal-transverse line. The appearance of sharp spots in the pole figure is a consequence of the large size of grains, reducing the number of orientations contributing to these pole figures. In the remaining left region, few g_{DF} (blue) grains, several g_{RX} (red) grains and an increased number of grains with the C3 orientation (green) are observed. The pole figures generated from this portion of the map are rather spotty due to the large grain size and are not presented here for space reasons.

Region B appears as a mixture of regions A and C, the grain boundary misorientation function is similar to that observed in region C (and the base material), but with a clear maximum at 60º. This peak at 60º indicates that some of the original α grains have transformed to β and then re-transformed to more than one α colonies. The soft background with the maximum at 30º indicates that a great portion of the original α grains remains with a similar orientation to that of the base material. Only small changes in the (0001) pole figure where observed between Regions B and C, indicating that texture memory is still active in this region.

We applied a β grain reconstruction algorithm to the EBSD image of Figure 9(a). This algorithm is based on the analysis of the misorientation between neighboring α grains looking for specific misorientation typical of two or more variants formed in the same β grain, through the orientation relationship. A nearest neighbor transformation and noise reduction method was employed similar to the method employed in [38,39] whereby 'votes' for a potential parent orientation are obtained by comparing potential parent orientations of the variant to that of neighboring variants. An angular tolerance of 5º was used for variant identification and 3º for common β parent identification. The algorithm can give false positive in case α grains have specific misorientation not related to β–>α transformation but to a statistical probability ruled by texture. It can also give false negative when only one variant is formed in each β grain, as in the case of texture memory during α–>α+β–>α transformation.

Figure 9(b) shows this β map, where β grains are shown in colors and white regions are α grains non-reconstructed as β by the algorithm. Table 2 shows the results of the analysis of Figures 9(a) and (b), where the total number of grains, mean area and major length average for these two maps are presented. In the

EBSD map of Figure 9(a), the number of α grains increases markedly when moving from Regions A to C. This is accompanied with a net decrease of the mean area of these grains. This occurs because Region A is characterized by the presence of Widmanstätten colonies with larger size (major size ~20μm) compared to the equiaxed grains of Region C.

On the reconstructed β image of Figure 9(b), two types of grains can be identified, reconstructed β grains (in colors) and non-reconstructed grains in white. Non-reconstructed grains could be non-transformed grains or grains that transformed to β and re-transformed to α by precipitation of only one variant. Reconstructed grains are β grains for which more than one variant nucleated during cooling. In Region A and also in that part of the HAZ to the left of this region, the algorithm successfully reconstructed β grains, excluding only few cases. In Region A, the surface fraction of α grains reconstructed as β is ~80% (see Table 2). This result indicates that β transformation was almost complete, and also that precipitation of more than one variant per β grain occurs during cooling. In Region B, a lower fraction of β grains (~25%) could be reconstructed. According to the microstructure of Figure 4(e), this region is characterized by the coexistence of non-transformed α grains and α grains with a parallel plate substructure. These last grains are probably formed through the precipitation of only one variant per β grain. This could explain the high rate of fails of the algorithm in this region. Finally, in Region C very few grains could be reconstructed as β. The observation of some α grains with a parallel plate substructure in the optical micrographs indicates that partial transformation occurs, but with a lower volume fraction. As in Region B, the algorithm could not associate these grains with a prior β grain.

Summarizing, from the analysis of the EBSD maps of Figure 9, we identified three regions in the interface with different characteristics. Region C, closer to the base material, where α grains did not transform or transformed to form α grains with a parallel plate substructure, and the texture is similar to that of the base material; Region B, where a small fraction of the material transformed to β and the texture is still similar to that of the base material; and Region A, close to the HAZ, where the material transformed almost completely to β and the final texture changes drastically compared to that of the base material. These results suggest that full β transformation seems to be a necessary condition for the development of the strong C3 texture.

4. Texture modelling

The evolution of texture across the welds is directly related to the phase transformation of α grains (h.c.p) to the high temperature β phase (b.c.c) during heating and subsequent re-transformation to α during cooling. During phase transformation, the transformed grains follow a precise crystallographic relation with the original grains aligning compact planes and directions of both phases. This is the Burgers orientation relation, where: β{110} // α{0001} and β <111> // α<11-20>. According to this crystal relation, there are a total of 6 possible variants during α->β transformation and 12 variants during β->α transformation [20].

The larger size of β grains compared to the original α grains suggests that during heating one or few β grains are nucleated in each α grain and also that significant grain growth occur at high temperatures, as shown in Figure 9(c). However, during cooling more than one α grain can nucleate in a β grain, with this number dependent on the cooling rate at the transformation temperature and on the β grain size [15, 40, 41]. A recent paper showed that in the extreme case of fast cooling rates and large β grain size, nucleation of all 12 α variants can occur in the same β grain [42]. In the region of the HAZ close to the welding pool, corresponding to fast cooling rates and large β grain size, up to 3 different α variants are commonly observed in each β grain. These nuclei grow to form colonies with the "basket weave" morphology and the misorientation of these variants are ~10º, ~60º or ~90º, as observed by EBSD [27]. In regions of slow cooling rates and fine β grains, like the region of the HAZ close to the base material, the number of α nucleus per β grain diminishes, and only few Widmanstätten colonies with the parallel plate morphology are formed in each β grain.

From the point of view of the evolution of texture, each α grain transforms during heating to one of the six possible variants available according to the Burgers relation, and then re-transforms during cooling in different oriented colonies of the twelve available variants, with the number of colonies per β grain dependent on the cooling rate (we disregard the extreme case of the 12 precipitation variants). Figure 10 shows schematically the evolution of texture expected for an α grain with the C2+ original orientation. At high temperature, a β grain with an orientation corresponding to one of the six transformation variants nucleates. To construct Figure 10(b) we have arbitrarily chosen one of these possible six. During the β–>α transformation, Burgers relation imposes a strong constraint to the available orientations of the *c*-axis of the transformed grain. All the α colonies that nucleate in this β grain should have their *c*-axis along one of the 6 poles shown in the (110) pole figure of Figure 10(b). In Figure 10(c) we have plotted the 3 variants observed, having a misorientation of 60º and [11-20] as a rotation axis. In this case three orientations observed in the HAZ appear as possible: C3 and g_{RX} (C2+, C2-).

We have evaluated the texture after such a double transformation for two initial ideal textures. To perform this calculation, we have summed the contribution of all possible transformation variants with equal probability. The aim is to identify the possible final α grains orientations after imposing the Burgers' relation. In Figure 11 we present in (a) the initial texture constructed as two Gaussian distribution of 15º width centered at the ideal g_{DF} components, in (b) the predicted β texture after applying the Burgers relation with the 6 variants with the same probability; and in (c) the re-transformed texture estimated from the β texture with no variant selection. Figure 12 shows a similar analysis but for an initial texture formed by Gaussian centered at the g_{RX} orientations.

The final texture after the double transformation for a g_{DF} as initial texture (Figure 11) shows a (0001) pole figure with two maxima associated to the C1- and C2+ orientations and other poles located along the TD-RD outer circle 30º rotated from the TD. Also there are some maxima located along the ND-RD line, shifted 30º from the RD. Some of these structures were not found in the experimental pole figures measured in the HAZ. Moreover, the (11-20) pole figure of Figure 11 shows a complete absence of a pole along the RD, which is clearly observed in all the (11-20) experimental pole figures of Figure 6. In a previous work, Santisteban et al [6]. have done a thorough study of this same weld by energy resolved neutron radiography at ISIS, UK. In their work, they studied the dependence of the total neutron cross section when the beam is parallel to the RD. From this cross section, they built maps showing the height of the (0002), (11-20) and (10-10) Bragg edges along the whole weld. They observed that inside the HAZ there is a sharp increase of the height of the (11-20) edge while at the same time the (10-10) edge practically vanishes. This was interpreted as an increase in the number of grains with their {11-20} planes parallel to the RD, and strong reduction in the number of grains with their {10-10} planes parallel to the RD inside the HAZ. This result is consistent with the development of a texture in the HAZ having an intense (11-20) pole along the RD shown in Figure 6.

On the other hand, the α texture predicted after cooling from an initial g_{RX} component (Figure 12) have all of the characteristics found in the experimental textures for the HAZ presented in Figure 6. The C3, C4 and C5 components, listed in Table 1 as the main orientations appearing at the HAZ, have its correspondence in these pole figures. Furthermore, these pole figures are almost identical to those found in the HAZ close to the fusion region. This shows that in order to reproduce the texture observed in the HAZ the contribution of the g_{DF} grains to the initial texture must be eliminated. This means that during some part of the transformation process, either heating before transformation, during transformation, or grain growth in the β phase, the contribution of grains which originally had these orientations must vanish.

It is interesting to note that although the pole figures of Figure 11 and 12 arise from the contribution of 6*12=72 variants, they can be described by the use of a reduced number of orientations (i.e. there are only 9 poles in the (0001) pole figure). For each α grain, a total of 72 different orientations are expected to appear after the double transformation, however, some of these orientations are identical due to the crystal symmetry of the phases. This reduces the number of non-equivalent orientations to 63. Moreover, some of the remaining 63 only differ in some degrees from one another [15,42]. The use of broad Gaussian distributions to simulate the initial texture in Figures 10 and 11 blurs the small orientation shifts originated by the different variants, resulting in a unique and broad structure. In this type of materials, the spread of orientations found around ideal texture components is in general of the order of 15º to 20º, so it is a common practice to interpret these textures in terms of broad distributions centered at a reduced number of orientations.

5. Discussion

In the previous sections we have described in detail the variations of microstructure and texture across the weld. Regarding the microstructural changes, we noticed that the equiaxed grain structure, typical of the recrystallized as-received material, changes to a Widmanstätten grain morphology in the HAZ and the welding pool. In the limit between the HAZ and the base material, we identified by optical microscopy and SEM a region of ~1mm width where equiaxed grains and grains with irregular shape without substructure coexist with Widmanstätten grains with parallel plate morphology. This region was associated to that part of the weld where the maximum temperatures were in the α+β region. The equiaxed grains and the grains with irregular shape without substructure were associated to non-transformed α grains, while Widmanstätten grains were associated to grains that underwent the α–>β–>α transformation. In the region of the HAZ where full β transformation occurred, the microstructure changes from Widmanstätten grains with a parallel plate morphology close to the base material to "basket weave" morphology close to the welding line. The transition from parallel plate to "basket weave" is smooth and is accompanied also by a decrease in the plate width, as shown in Figure 5. These microstructural changes were interpreted in terms of the dependence with the distance to the welding line of the β grain size and cooling rate at the β–>α transformation temperature (~950ºC). The "basket weave" morphology appears in regions of fast cooling rates and coarse β grains (closer to the welding line) while the parallel plate morphology appears in regions of fine β grains and slow cooling rates (close to the base material).

On the other hand, texture also changes across the weld. Three experimental methods (neutrons, X-Ray and electron diffraction) were used to characterize the texture variation at different length-scales. Neutron diffraction is useful in places where the grain size is large, especially in the HAZ close to the welding line, however the size of the samples used in this experiment were of several millimeters. High energy X-ray diffraction in transmission geometry was exploded to characterize texture variations as a function of position with a spatial resolution of ~300μm. Through this experiment, the different textures appearing along the HAZ could be clearly determined for GTAW and PAW methods, as illustrated in Figure 6. Comparison of HE-XRD and neutron results shows excellent agreement, giving confidence to the experimental method in regions of large grain sizes. Finally, electron diffraction (EBSD) was used to elucidate texture changes at the narrow interface of ~1mm width adjacent to the base material.

Summarizing the main results, texture undergoes different changes from the base material to the welding line, all of them associated to the α–>β–>α transformation. At the interface region, where only partial transformation occurred, the texture remains similar to that of the base material. This behavior was associated to a texture memory effect. Within the HAZ, adjacent to the interface, there is a region of ~2mm width where the texture is dominated by the C3 component (*c*-axis of the hexagons parallel to the transverse direction). Moving towards the welding line, other texture components show up (C2 and C4). The intensity of these components depends on the distance to the center of the weld.

From the EBSD results of Figure 9 and the analysis based on texture modelling of Figure 11 and 12, we can propose that in order to explain the texture changes observed in the HAZ three conditions are necessary: 1) if the maximum temperature is below the β transus, as in the interface region, a texture memory effect activates, if this temperature exceeds the β transus, from the welding pool up to the interface region, there is no texture memory effect; 2) grains with the g_{DF} component, which are the most frequently found in the base material, must vanish before transformation, during the α–>β transformation or as β grains. This is necessary to explain the appearance of an intense (11-20) pole along the RD in the final texture. 3) In the region of the HAZ where full β transformation occurred (from the interface region to the welding pool), there is variant selection during the β–>α transformation. This variant selection is strong close to the interface region (responsible for the sharp C3 texture), and relaxes as one moves towards the welding line. In particular, the texture close to the fusion pool is similar to that obtained in Figure 12 assuming no variant selection, so weak or null variant selection is expected near the welding line.

Regarding point 2), the weakening of the g_{DF} component during heating has been reported to occur in cold rolled Zircaloy-2 [13], and in cold rolled Ti [9] before the onset of the α–>β transformation. The initial texture of these cold rolled materials is dominated by a strong g_{DF} component and a weak g_{RX} component. In the first work texture was followed in situ during recrystallization and transformation to the α+β region of Zircaloy-2 by X-Ray diffraction of a high energetic beam (88 KeV). At 795ºC (before the onset of the α–>β transformation) the α texture is dominated by g_{RX}, showing a very weak g_{DF} component. After transformation to the α+β phase, the experimental β texture results are almost identical to that presented in Figure 12. In the second work, the recrystallized Ti material shows a texture dominated by the g_{RX} component at 800ºC (before transformation), and a transformed β texture also similar to that shown in Figure 12. In a more recent paper, Zhu et al. [36] analyzed the evolution of texture of a Zr-2Hf alloy during deformation, recrystallization and grain growth for annealing temperatures in the α range. They observed that while the deformed material has a higher amount of grains with the g_{DF} orientation compared to the g_{RX} orientation, at the end of recrystallization these two components appear with a similar proportion. The net increase of the g_{RX} component occurs at the end of recrystallization and during subsequent grain growth. They proposed that g_{DF} grains have higher stored energy compared to g_{RX} grains, favoring the migration of boundaries induced by strain (SIBM mechanism), producing in turn a net increase of the cleaner g_{RX} component at the expense of the g_{DF} component. In our case, Zircaloy-4 plates in the as-received condition are fully recrystallized, so the weakening of the g_{DF} components must be related to preferential grain growth at high temperature, as explained by Zhu et al.[36] or to preferential transformation of the g_{RX} during α–>β due to their higher stored energy. During welding, the time at temperatures before the onset of the α–>β transformation is too short to have extended grain growth, so we propose that the main mechanism operating is preferential transformation of the g_{RX}.

In the region of the HAZ where full β transformation occurred, the evolution of texture is interpreted in terms of a strong variant selection close to the interface region, and a weak variant selection close to the welding pool. Variant selection mechanisms in Ti and Zr alloys during α –> β –> α phase transformation have been linked to either the effect of strong plastic deformation at high temperature [43], to selective nucleation in β grains with particular misorientation [15], and finally to the interaction between transformation strain and elastic anisotropy of the β phase at high temperature [10, 16, 19], . This last variant selection criterion was applied to explain the inherited texture in the case of Zircloay-4 rod during α–>β–>α transformation with good success [16].

We consider that the first mechanism, associated to strong plastic deformation of the material at high temperature, as in hot rolling processes, is not applicable to our case. In fusion welds, the degree of plastic deformation at high temperatures is low, just given by thermal expansion, with strain values close to the elastic range (~1%). These values are far from the 60% strain necessary to activate this mechanism according to [43].

The second proposal to explain variant selection during β–>α transformation is based on observations of the misorientation between reconstructed neighboring β grains from α grains of the sharp texture component. Nucleation of α seems to occur with higher probability in grain boundaries of β grains that have nearly the same orientation or orientations related by the orthorhombic symmetry [13, 44]. It is supposed that this condition minimizes the surface energy of the embryo. This mechanism could be active; however we believe that it is not sufficient to explain the development of a strong texture dominated by the C3 component. This strong texture may be associated to a macroscopic asymmetry of the material, which favors the development of texture with the c-axis of the hexagons along the TD. However we consider that this must be studied in detail in future works.

The last mechanism is related to the elastic energy produced by the misfit strain between the α and β phases. According to classical nucleation theory, the rate of nucleation of a spherical nuclei able to overcome the nucleation barrier is $I \sim \exp(-\Delta G^{a}/kT)$, with ΔG^{a} the activation free energy barrier:

$$\Delta G\mathrm{a} = \frac{16\pi\gamma^3}{3(\Delta G_{chem} - w)^2} \qquad (1)$$

Where ΔG_{chem} is the chemical energy which depends on the under cooling, w s is the elastic strain energy and γ is the surface energy of the embryo.

In an unconstrained single β crystal, the transformation to α involves a 10% contraction along one of the β <110> directions and 2% contraction and 10% expansion along the two perpendicular β <110> directions [26]. In a polycrystalline material, such transformation strains can create very significant elastic strain energies that could be minimized by the selection of certain α variants. In a first approximation, the energy density increase due to the α embryo is approximated by [16]:

$$w = \frac{1}{2}.\varepsilon^B{:}C{:}\varepsilon^B \qquad (2)$$

where C is the elastic tensor of the β phase and ε^B is the transformation strain tensor of a given variant expressed in the macroscopic reference system. The elastic anisotropy of the β phase, due to the texture and elastic anisotropy of the single β crystal, is responsible for different w values among the variants. According to (1), variants with the lowest w will have the highest nucleation rate. For small undercooling, ΔG_{chem} is small and the nucleation rate of the more favorable variant will be much higher than the rest. For high undercooling ΔG_{chem} is large compared to w and then all variants will have similar nucleation rate.

For continuous cooling with slow cooling rate, nuclei of the most favorable variant precipitate first and growth over the β grain. For fine β grains, transformation to α can be completed before undercooling is high enough to activate the nucleation of other variants. Then, strong variant selection occurs. For high cooling rates, and coarse β grains, transformation to α is incomplete, and high undercooling activates the nucleation of the less favorable variants. Then, weak variant selection occurs.

To evaluate Eq. (2) the misfit strain tensor of each variant, forming in a particularly oriented β grain, must be expressed in the sample reference system before making the contraction with the elastic tensor of the matrix. This means, that independently of the orientation of the β grain, *w* only depends on the orientation of the variant expressed in the sample reference system. Therefore, variants precipitated in different β grains with similar orientations (for example C3 orientation) must have similar *w* values. It is then plausible that this variant selection criterion explain the development of the strong texture dominated by the C3 component. To do so, it is necessary to know in detail the texture of the β phase. This will be studied in more detail in future works

Based on these ideas, the changes in the HAZ of both texture and microstructural can be interpreted in the following way: in the interface region, the peak temperature is below the β transus, a texture memory effect activates and the material ends with the same texture as the base material. In the region of the HAZ next to the interface, where the peak temperature surpasses the β transus, the variant selection criterion proposed above is active. In this region and due to the relative slow cooling rates and fine β grains there is a strong variant selection that favors the formation of the C3 component. The morphology of the grains is mainly parallel plate with wide plate thickness and majorly one or two colonies are created within the prior β grains. Close to the welding pool, high cooling rates and coarse β grains give rise to weak variant selection and the formation of the ”basket weave” morphology. In between these two regions, the continuous changes in cooling rate and β grain size with position implies a continuous variation of the strength of variant selection and grain morphology, as clearly seen in the spatial variations of the microstructure of Figure 4 and 5, and of texture of Figure 6.

6. Conclusions

We presented a detailed characterization of the microstructural and crystallographic texture changes along two welds of Zircaloy-4 plates. The equiaxed grain structure, typical of the recrystallized as-received material, changes to a Widmanstätten grain morphology in the HAZ and the welding pool. In the limit between the HAZ and the base material, we identified by optical microscopy and SEM a region of ~1mm width where equiaxed grains coexist with grains with internal structures (the interface). This region was associated to that part of the weld where the maximum temperatures were in the α+β region. Three complementary experimental methods (neutrons, X-Ray and EBSD) were used to characterize the texture variations in different length-scales of the HAZ. All these changes could be associated to the α–>β–>α transformation.

A texture "memory" effect was observed in the interface, where the maximum temperatures were in the α+β region. In the rest of the HAZ important texture variations were observed. In order to explain these texture changes three conditions are necessary: 1) the maximum temperature must surpass the β transus,; 2) grains with the g_{DF} component, which are the most frequently found in the base material, vanish during the α–>β transformation or as β grains. 3) There must be a strong variant selection during the β–>α transformation in the region of the HAZ close to the base material, and a continuous relaxation of the strength of this variant selection as moving towards the welding line.

Based on differences in the nucleation energy of the different transformation variants we associated the observed changes of both microstructure and texture to the dependence of the cooling rate and β grain size with position. Fast cooling rates and large β grains were associated to weak variant selection and high nucleation rates resulting in "basket weave" morphology, while slow cooling rates are linked to strong variant selection and low nucleation rates resulting in the parallel plate morphology.

Acknowledgement

This research was partially funded by CONICET under PIP-542-2011, and by IAEA under Research Contract 17252 "Kinetics of hydride precipitation under applied stresses on Zr-based alloys" which form part of the CRP F12024 entitled "Utilisation of accelerator-based real-time and in-situ methods in investigation of materials for energy applications: CRP code: F12024". Usage of the Advanced Photon Source was supported by the U.S. Department of Energy, under Contract No. DE-AC02-06CH11357.

The authors acknowledge the *Laboratorio de Microscopía Electrónica y Microanálisis* (LAMARX) of the Universidad Nacional de Córdoba, Argentina, where EBSD measurements were carried out.

Figures

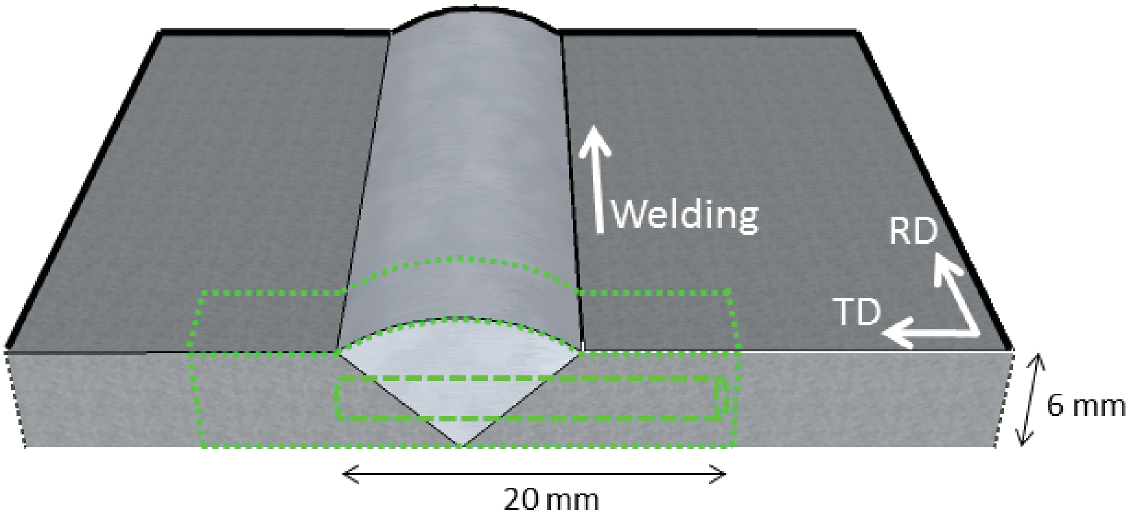

Figure 1. Scheme of the GTAW weld. The green dashed lines indicate the places where the coupons for the microstructure characterization and XRD experiment were extracted.

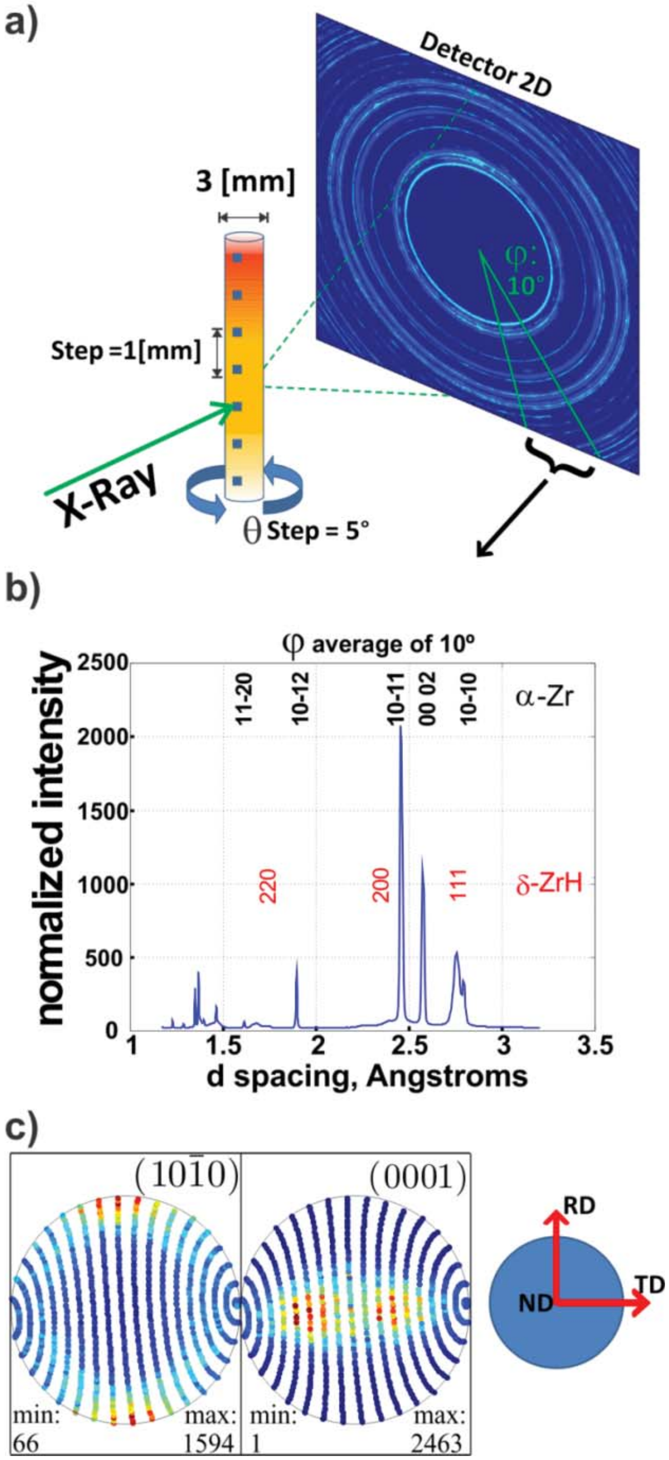

Figure 2. a) Scheme of the experimental setup. The X-Ray beam goes through the entire thickness of the cylindrical sample and the diffracted cones are collected by a CCD detector placed 1.8m behind. b) Typical diffractogram obtained after averaging a 10º polar section of the image. Peaks corresponding to the two phases present (αZr and δ hydride) are identified. c) Complete experimental pole figures constructed after data processing and plotting convention.

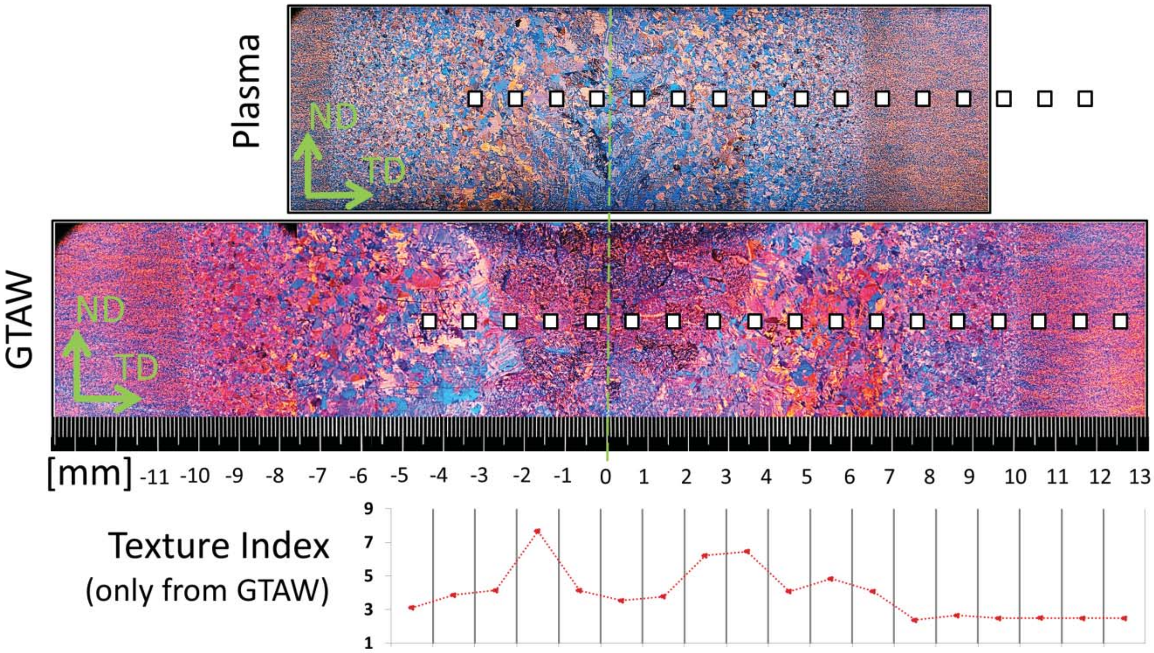

Figure 3. Panoramic micrograph under polarized light of PAW and GTAW welds, the different colours highlights different orientations of the grains. White squares indicate the position and illuminated area of the X-ray beam. Texture index calculated from the ODFs is shown in the bottom figure for GTAW.

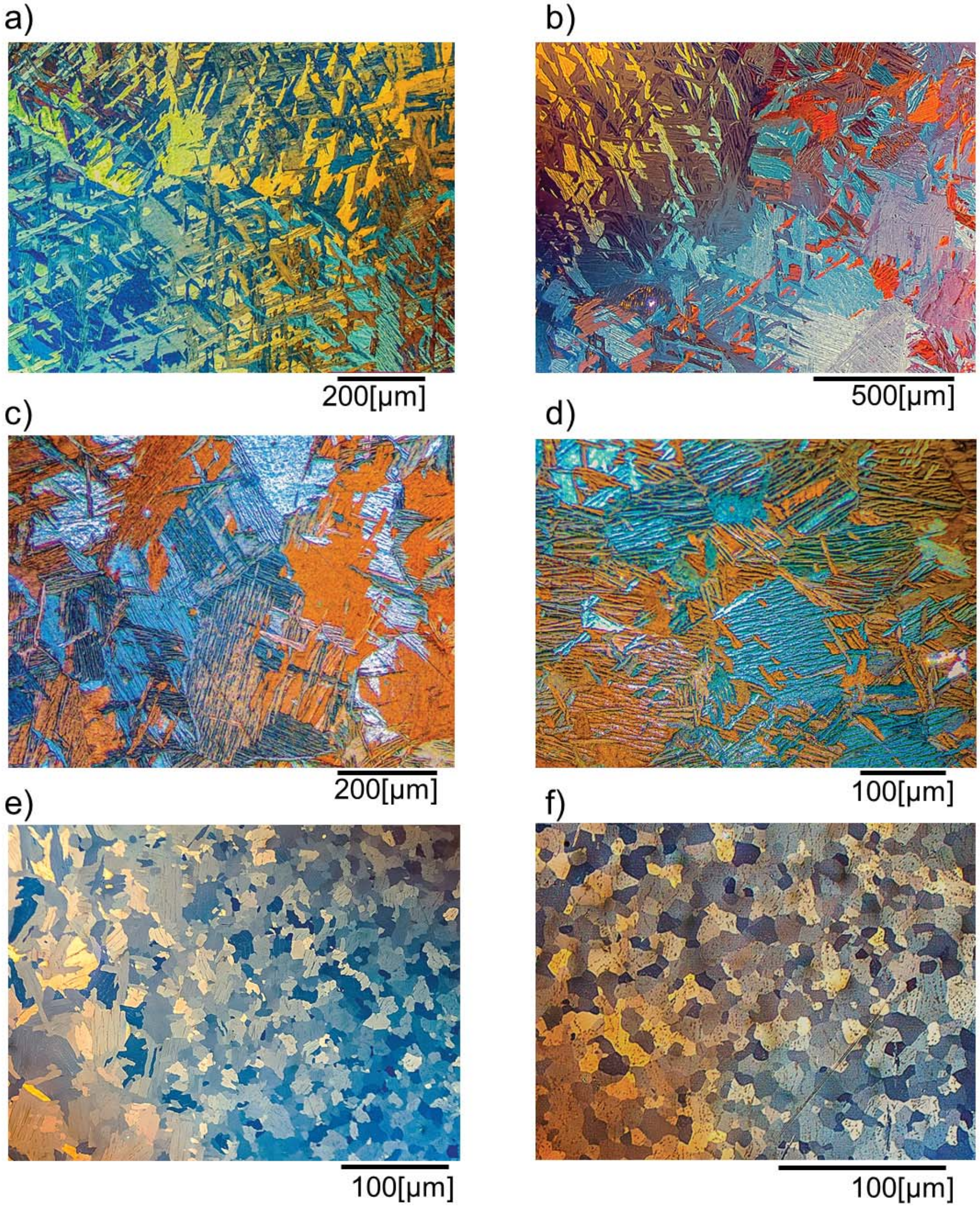

Figure 4. Micrographs under polarized light at different positions in the GTAW sample. a) at 0mm (weld centre), b) at 3mm, c) 5mm, d) 9 mm, e) 10mm from the weld centre; and f) base material.

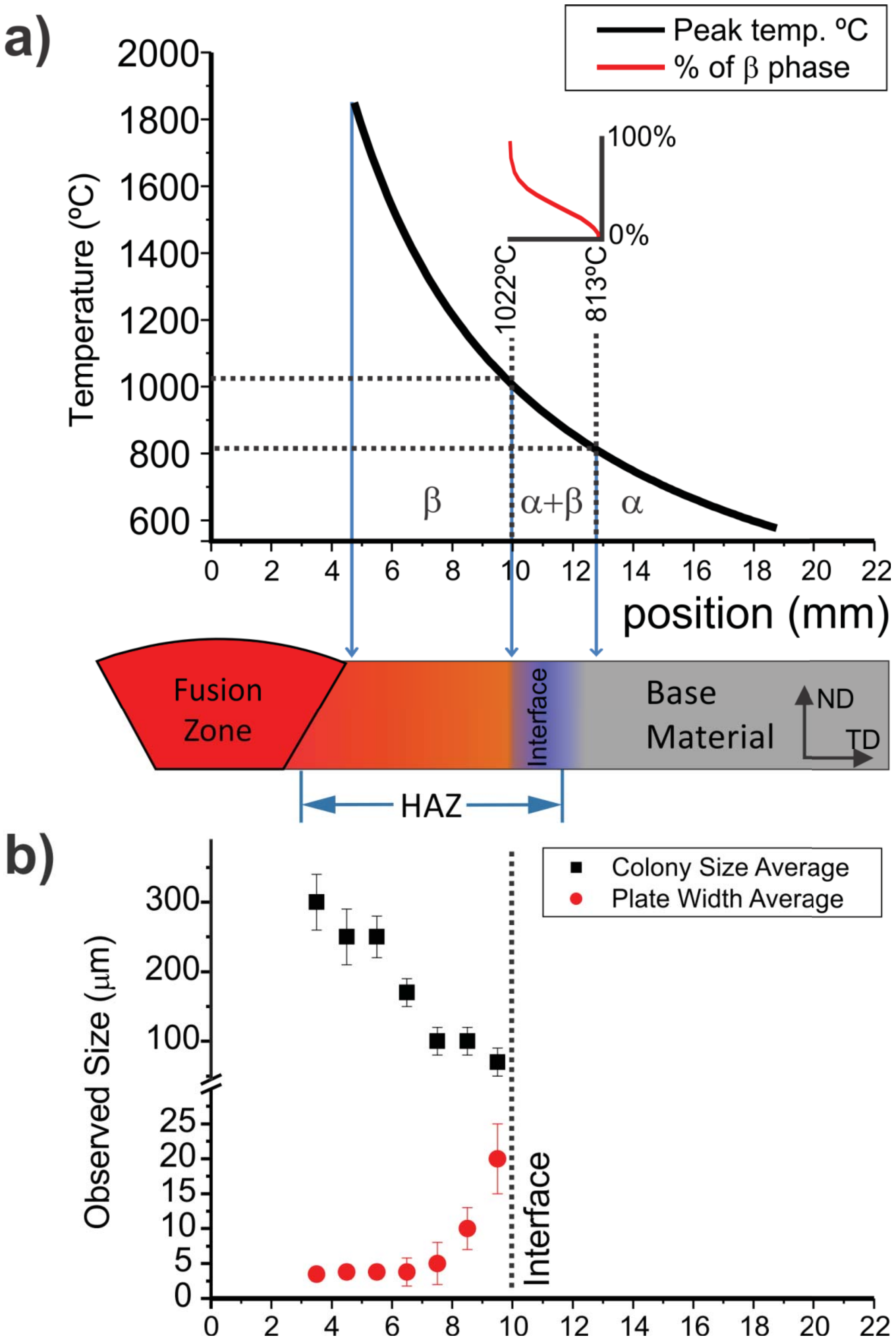

Figure 5. a) Peak temperature gradient across the transversal direction of the weld sample and equivalent fraction of β phase transformation (equilibrium case) as function of position, taken from Forgeron et al [29]. b) Colony and plate width sizes of the Widmanstatten grains in the HAZ from optical observation

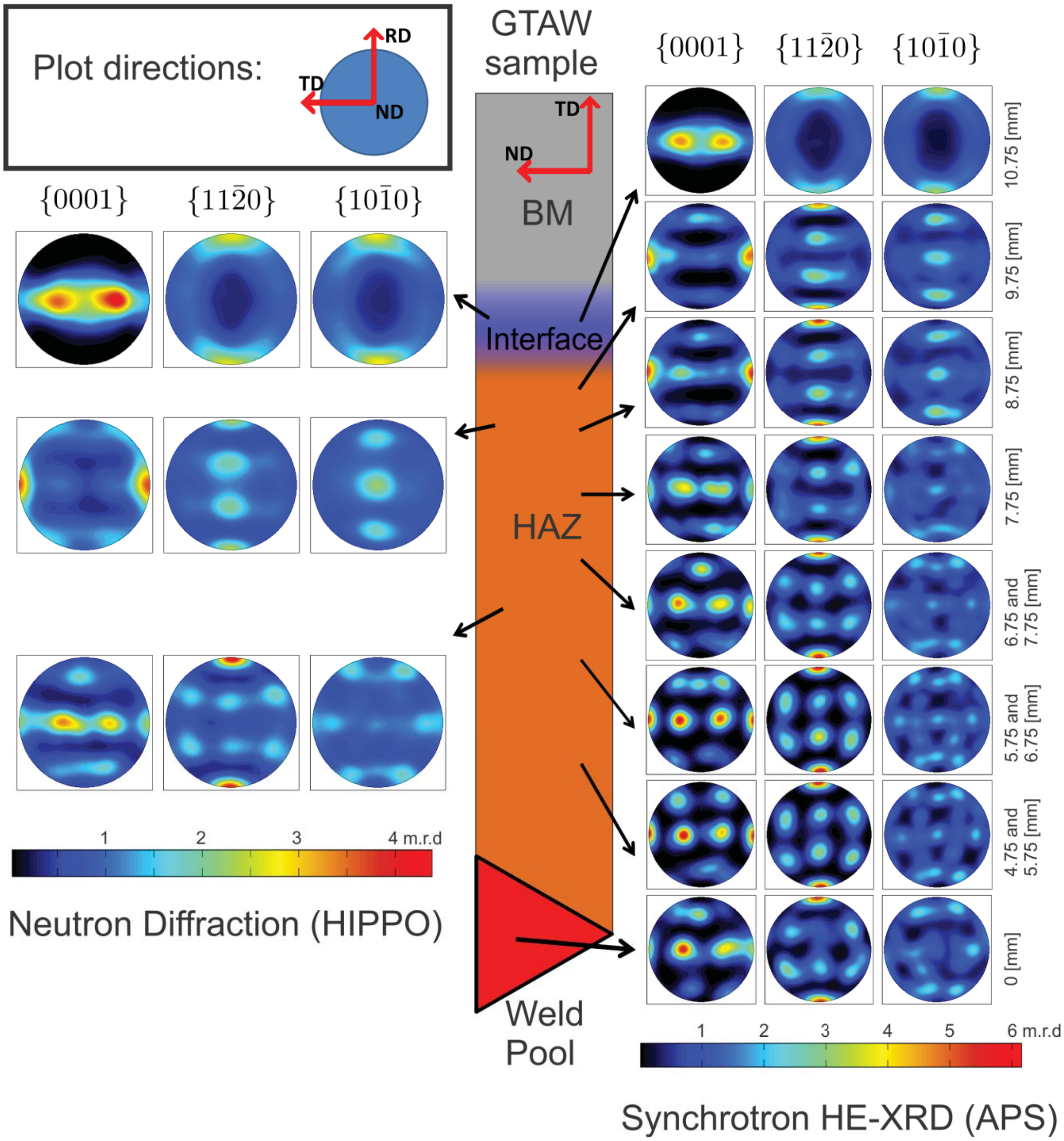
Plot directions:
RD
TD
ND
GTAW sample
BM
Interface
HAZ
Weld Pool
{0001}
{11$\bar{2}$0}
{10$\bar{1}$0}
10.75 [mm]
9.75 [mm]
8.75 [mm]
7.75 [mm]
6.75 and 7.75 [mm]
5.75 and 6.75 [mm]
4.75 and 5.75 [mm]
0 [mm]
1
2
3
4 m.r.d
Neutron Diffraction (HIPPO)
1
2
3
4
5
6 m.r.d
Synchrotron HE-XRD (APS)

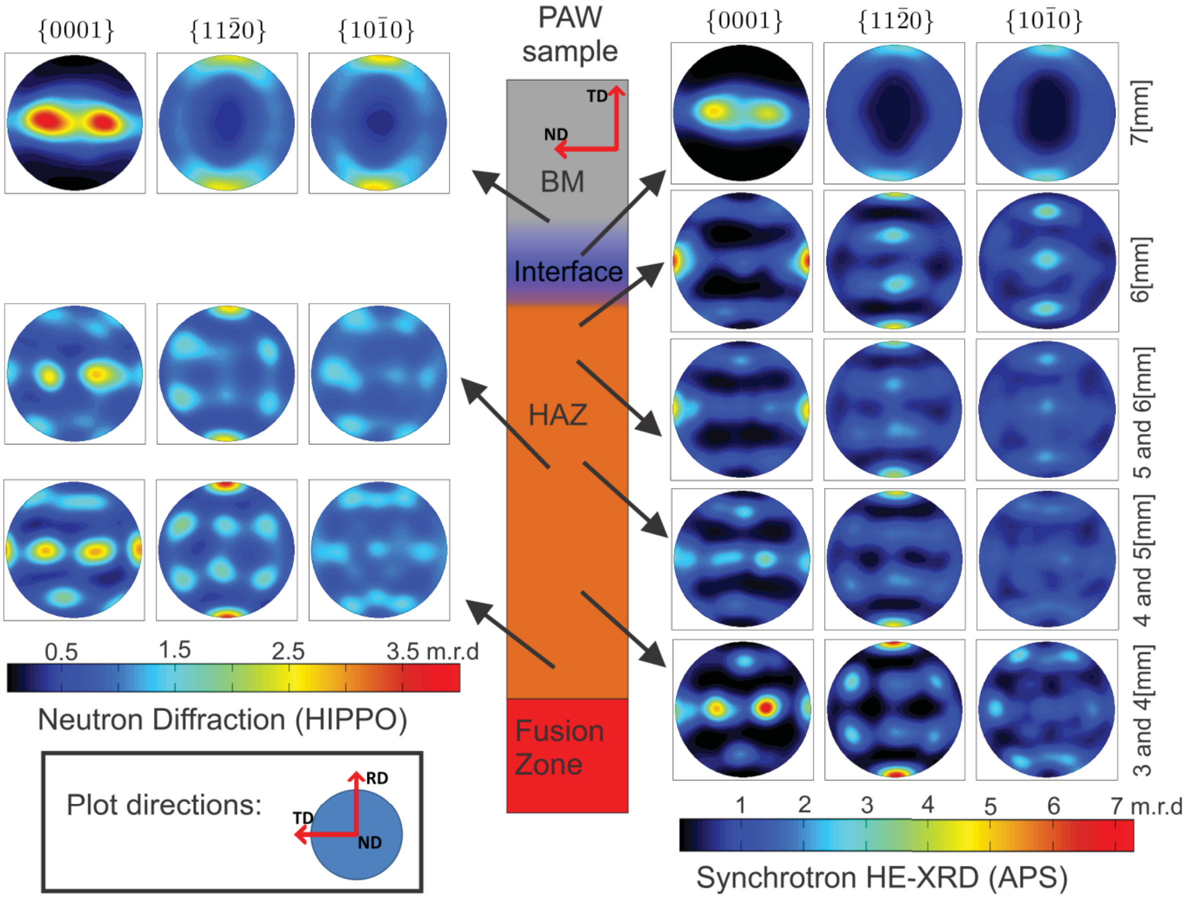

Figure 6. Evolution of texture across the welds: a) GTAW b) PAW. The pole figures at the right were determined by HE-XRD at APS. Those at the left were measured by Neutron Diffraction, taken from ref [6].

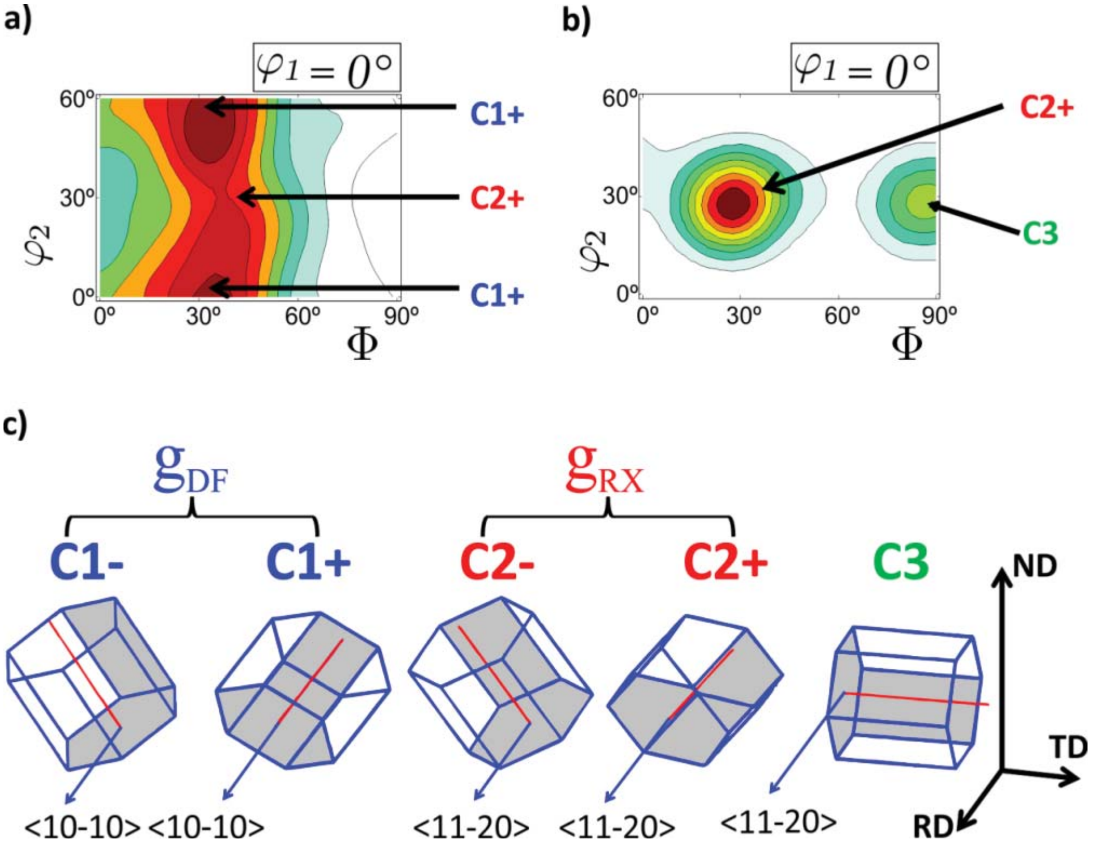

Figure 7: φ_1=0º section of the ODF obtained at: a) base material and b) HAZ (position 3and 4 mm of PAW sample). c) Hexagonal crystals of the principal orientation components in the sample reference system.

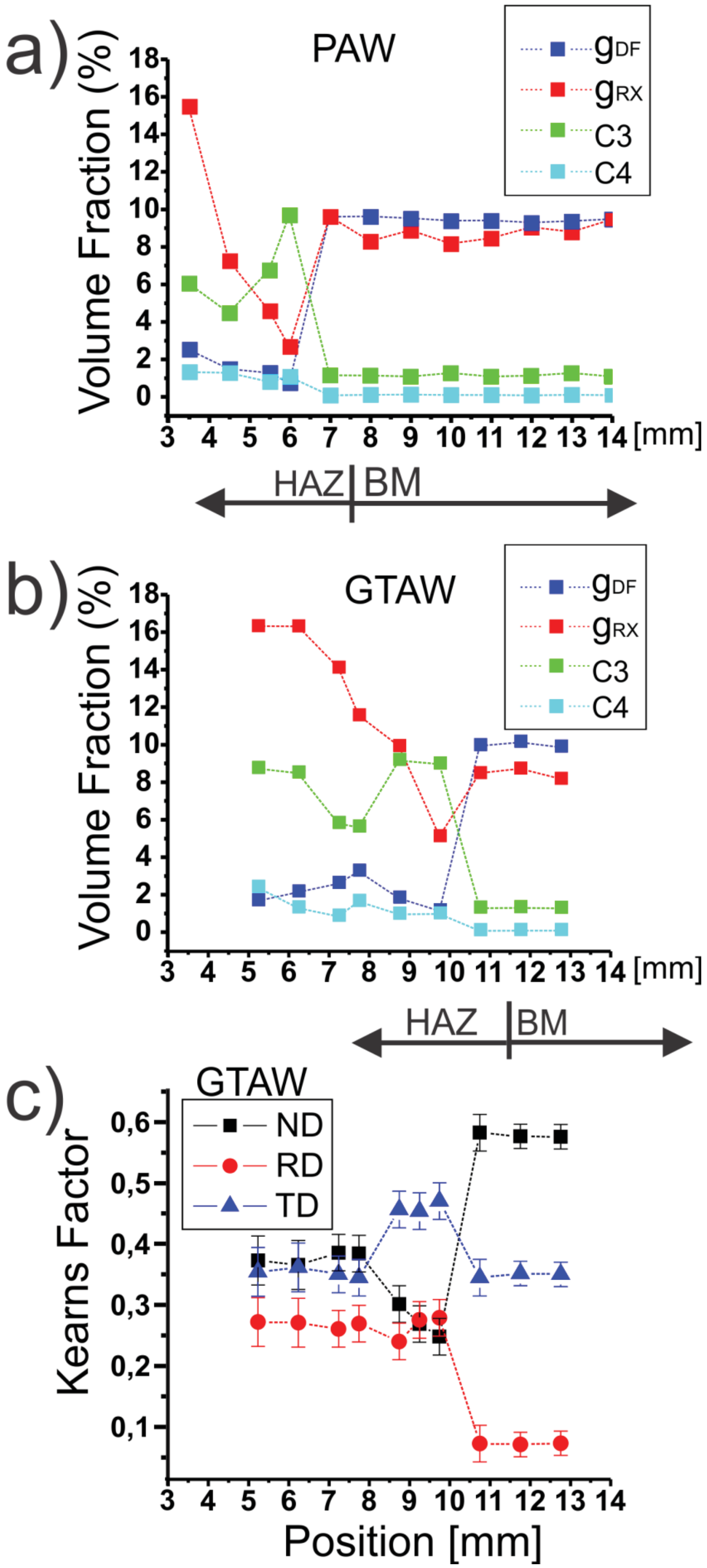

Figure 8. Volume fractions of the main texture components presented in Table 1, for a) PAW , b) GTAW . c) Kearns factors (only for GTAW sample) calculated from the (0001) pole figures of fig. 6(a)

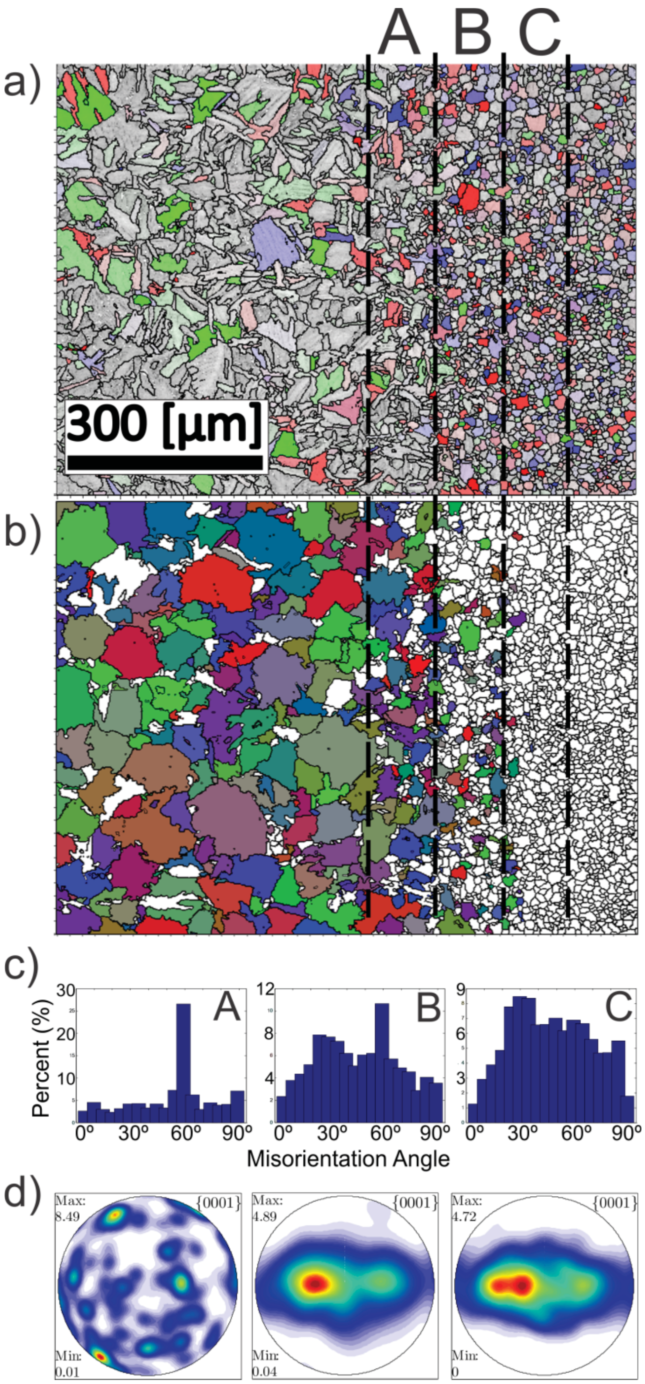

Figure 9. a) Orientation map of the interphase zone, at 10mm from the weld centre (GTAW sample). Grains in colours correspond to g_{DF}(blue), g_{RX}(red) and C3 (green). b) prior β grains reconstructed from a), in white untransformed α grains or non-reconstructed as β . c) α grains boundary misorientations angle distribution for regions A, B, C. d) (0001) pole figures for regions A,B,C.

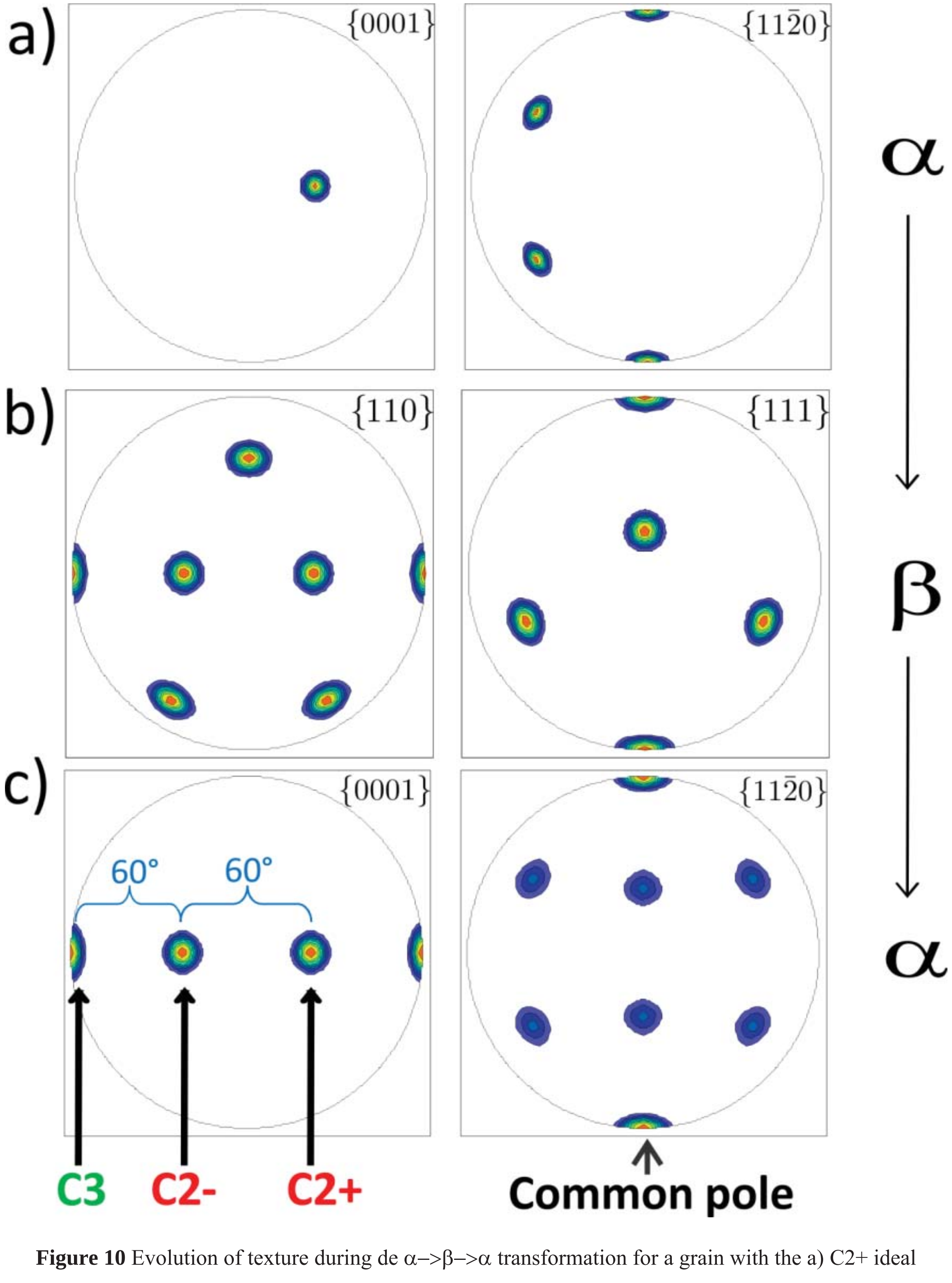

Figure 10 Evolution of texture during de α–>β–>α transformation for a grain with the a) C2+ ideal orientation following the BOR. b) β texture obtained using one variant during α→β. c) α texture after β→α using 3 variants with misorientation angles of 60°.

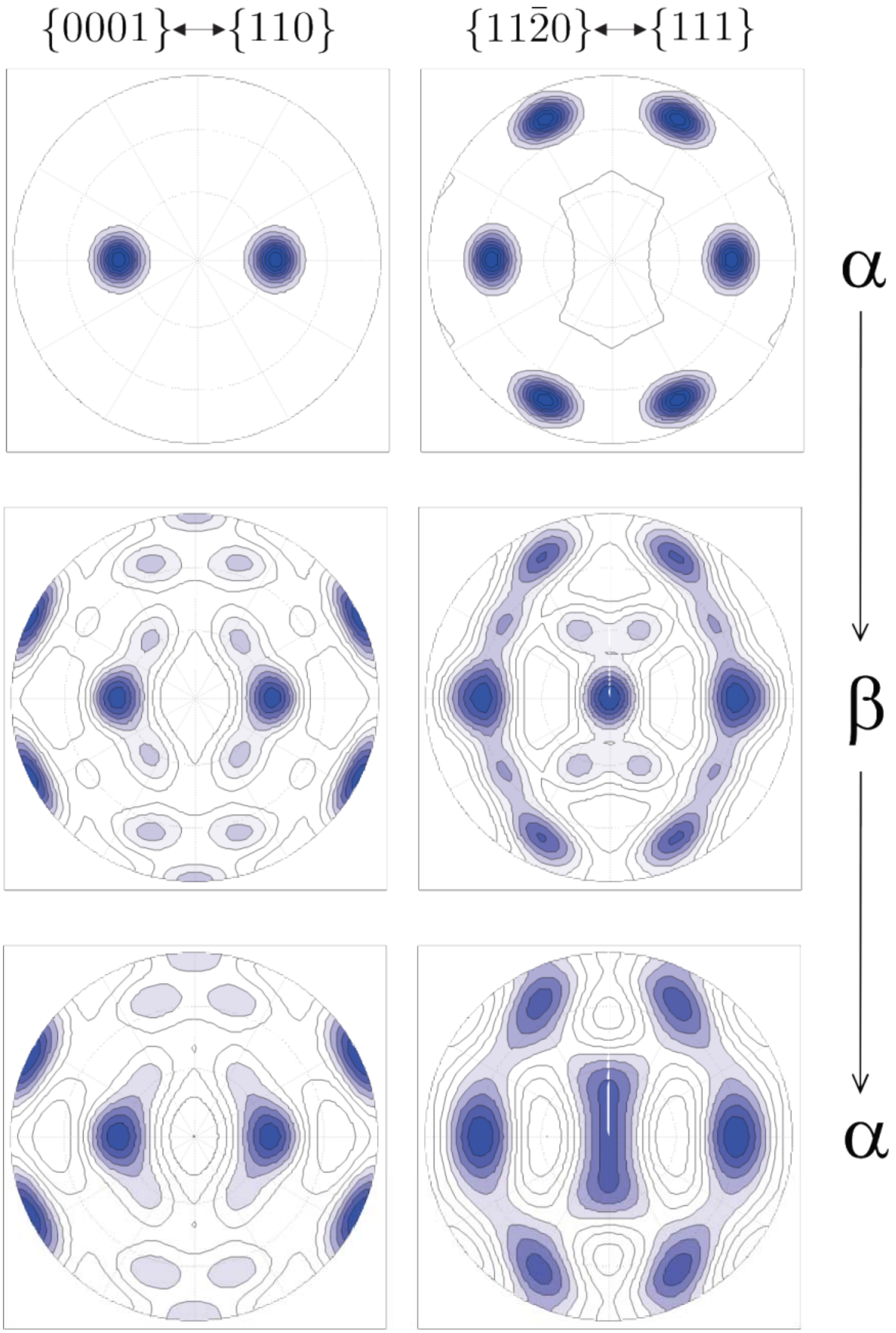

Figure 11 Calculated pole figures for a complete α β α transformation for an initial texture corresponding to a g_{DF} ideal orientation, with no variant selection.

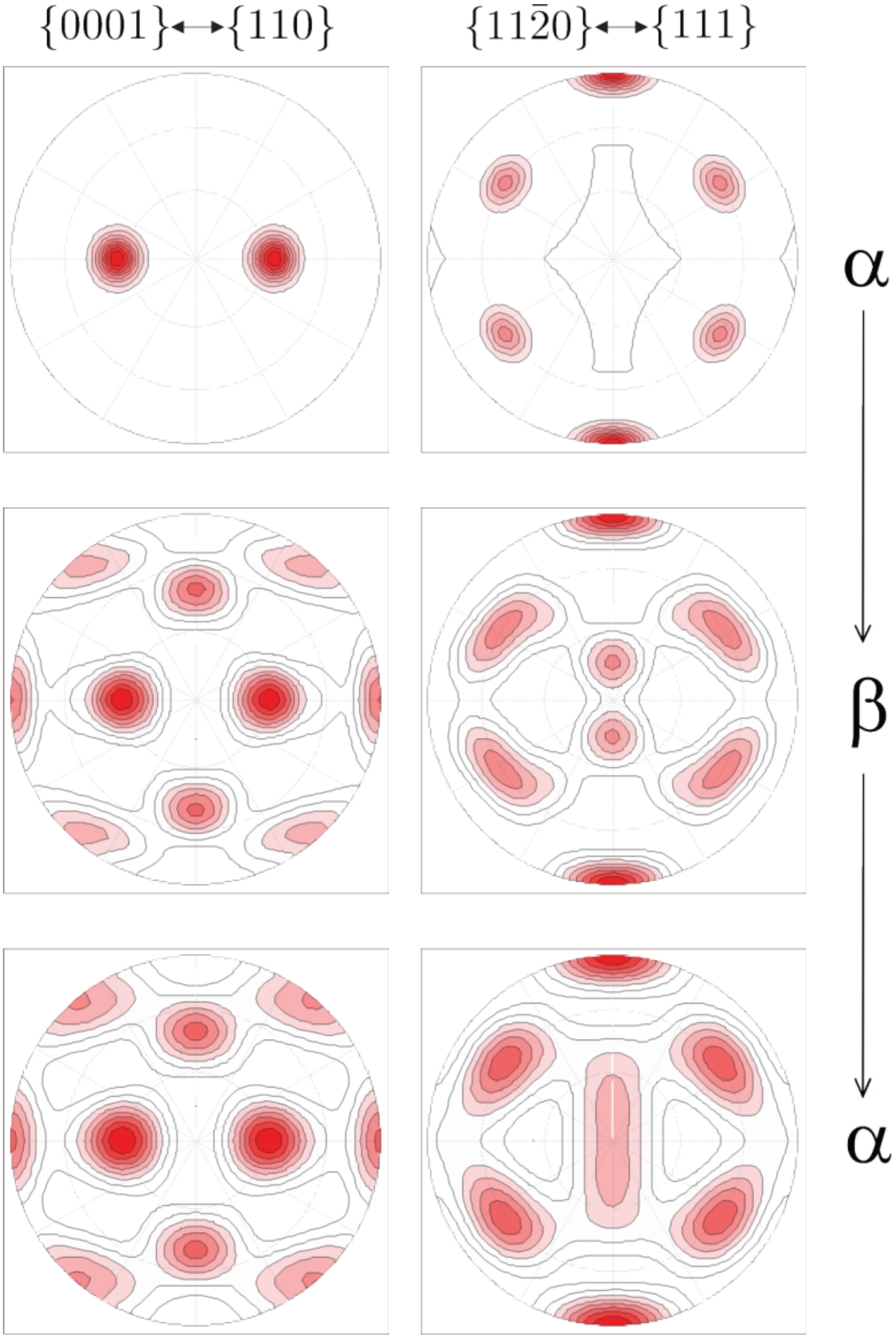

Figure 12. Calculated pole figures for a complete α β α transformation for an initial texture corresponding to a g_{RX} ideal orientation, with no variant selection.

Tables

Component		φ_1	φ	φ_2
g_{DF}	C1+	0º	30º	0º
	C1-	180º	30º	0º
g_{RX}	C2+	0º	30º	30º
	C2-	180º	30º	30º
C3		0º	90º	30º
Weak components	C4	270º	54.75º	5.25º
		90º	54.75º	5.25º
	C5	58.5º	73.25	10º
		121.5º	73.3	50º

Table 1: Main orientation components observed on both samples (Bunge rotation convention)

Region	Map	Type of Grain	Total Number	Mean Area [µm^2]	Major size Average [µm]	Surface fraction
A	α map (Fig 9(a))	α	499	143,7	19,5	-
	β map (Fig 9(b))	Non-reconstructed (α grains)	150	88,9	14,7	18%
		Reconstructed as β	100	584,0	36,2	82%
B	α map (Fig 9(a))	α	961	74,6	12,7	-
	β map (Fig 9(b))	Non-reconstructed (α grains)	699	76	13,8	75%
		Reconstructed as β	117	158	19,3	25%
C	α map (Fig 9(a))	α	958	75	12.6	-

Table 2: Grain statistic of the EBSD maps of figure 9.for the three regions A,B and C.

References

---

1 A. Miquet, D. Charquet, C. Michaut, C.H. Allibert, Effect of Cr, Sn and O contents on the solid state phase boundary temperatures of zircaloy-4, Journal of Nuclear Materials. 105 (1982) 142–148.

2 T.E. Perez, M.E. Saggese, Welding structures in gas tungsten arc-welded Zircaloy-4, Metallography. 15 (1982) 43–52.

3 C.E. Coleman, G.L. Doubt, R.W.L. Fong, J.H. Root, J.W. Bowden, S. Sagat, et al., Mitigation of harmful effects of welds in zirconium alloy components, Atomic Energy of Canada Ltd., 1993.

4 A.S.-R. John H. Root, Neutron Diffraction Measurement of Texture Variations Near a Weld in a Zr-2.5% Nb Plate, Textures and Microstructures. 14 (1991). doi:10.1155/TSM.14-18.989.

5 D.G. Carr, M.I. Ripley, T.M. Holden, D.W. Brown, S.C. Vogel, Residual stress measurements in a zircaloy-4 weld by neutron diffraction, Acta Materialia. 52 (2004) 4083–4091.

6 J.R. Santisteban, M.A. Vicente-Alvarez, P. Vizcaino, A.D. Banchik, S.C. Vogel, A.S. Tremsin, et al., Texture imaging of zirconium based components by total neutron cross-section experiments, Journal of Nuclear Materials. 425 (2012) 218–227. doi:10.1016/j.jnucmat.2011.06.043.

7 N.A.P. Kiran Kumar, J.A. Szpunar, Z. He, Microstructural studies and crystallographic orientation of different zones and δ-hydrides in resistance welded Zircaloy-4 plates, Journal of Nuclear Materials. 414 (2011) 341–351. doi:10.1016/j.jnucmat.2011.03.027.

8 K. Une, S. Ishimoto, Crystallographic measurement of the β to α phase transformation and δ-hydride precipitation in a laser-welded Zircaloy-2 tube by electron backscattering diffraction, Journal of Nuclear Materials. 389 (2009) 436–442. doi:10.1016/j.jnucmat.2009.02.033.

9 I. Lonardelli, N. Gey, H.-R. Wenk, M. Humbert, S.C. Vogel, L. Lutterotti, In situ observation of texture evolution during α→β and β→α phase transformations in titanium alloys investigated by neutron diffraction, Acta Materialia. 55 (2007) 5718–5727. doi:10.1016/j.actamat.2007.06.017.

10 M.R. Daymond, R.A. Holt, S. Cai, P. Mosbrucker, S.C. Vogel, Texture inheritance and variant selection through an hcp–bcc–hcp phase transformation, Acta Materialia. 58 (2010) 4053–4066. doi:10.1016/j.actamat.2010.03.012.

11 H.-R. Wenk, I. Lonardelli, D. Williams, Texture changes in the hcp→bcc→hcp transformation of zirconium studied in situ by neutron diffraction, Acta Materialia. 52 (2004) 1899–1907. doi:10.1016/j.actamat.2003.12.029.

12 J. Romero, M. Preuss, J. Quinta da Fonseca, Capturing the texture changes in a zirconium alloy during the allotropic phase transformation, Scripta Materialia. 61 (2009) 399–402. doi:10.1016/j.scriptamat.2009.04.031.

13 J. Romero, M. Preuss, J. Quinta da Fonseca, Texture memory and variant selection during phase transformation of a zirconium alloy, Acta Materialia. 57 (2009) 5501–5511. doi:10.1016/j.actamat.2009.07.046.

14 G.C. Obasi, R.J. Moat, D.G. Leo Prakash, W. Kockelmann, J. Quinta da Fonseca, M. Preuss, In situ neutron diffraction study of texture evolution and variant selection during the α→β→α phase transformation in Ti–6Al–4V, Acta Materialia. 60 (2012) 7169–7182. doi:10.1016/j.actamat.2012.09.026.

15 N. Gey, M. Humbert, Characterization of the variant selection occurring during the a-b-a transformation on titanium, Acta Materialia 50 (2002) 277–287

---

16 M. Humbert, N. Gey, Elasticity-based model of the variant selection observed in the β to α phase transformation of a Zircalloy-4 sample, Acta Materialia. 51 (2003) 4783–4790. doi:10.1016/S1359-6454(03)00318-5.

17 C. Cayron, Importance of the α→β transformation in the variant selection mechanisms of thermomechanically processed titanium alloys, Scripta Materialia. 59 (2008) 570–573. doi:10.1016/j.scriptamat.2008.05.013.

18 N. Gey, E. Gautier, M. Humbert, A. Cerqueira, J.L. Bechade, P. Archambault, Study of the α/β phase transformation of Zy-4 in presence of applied stresses at heating: analysis of the inherited microstructures and textures, Journal of Nuclear Materials. 302 (2002) 175–184.

19 Gey, N., Humbert, M., Gautier, E., Béchade, J.L., 2004. Study of the β→α variant selection for a zircaloy-4 rod heated to the β transus in presence or not of an axial tensile stress. Journal of Nuclear Materials 328, 137–145. doi:10.1016/j.jnucmat.2004.03.003

20 Burgers WG. “On the process of transition of the cubic-body-centered modification into the hexagonal-close-packed modification of zirconium”. Physica, 1943:1, 561.

21 L. Ortiz, R. Martinez, Zircaloy Welding in OPAL Reactor Reflecor Vessel, 15th Pacific Basin Nuclear Conference, Sydney, 2006.

22 A.V. Flores, A.G. Gomez, G.A. Juarez, N. Loureiro, R.I. Samper, J.R. Santisteban, et al., Typical Zirconium Alloys Microstructures in Nuclear Components, Practical Metallography. 51 (2014) 656–674.

23 M.A. Vicente Alvarez, J.R. Santisteban, G. Domizzi, J. Almer, Phase and texture analysis of a hydride blister in a Zr–2.5%Nb tube by synchrotron X-ray diffraction, Acta Materialia. 59 (2011) 2210–2220. doi:10.1016/j.actamat.2010.12.024.

24 E. Steffano, L. Schiffini, Chapter3 - Profile fitting and analytical functions, In Defect and Microstructure Analysis by Diffraction, Oxford University Press, 1999, p29-40.

25 F. Bachmann, R. Hielscher, H. Schaeben, Texture Analysis with MTEX – Free and Open Source Software Toolbox, Solid State Phenomena. 160 (2010) 63–68.

26 R.A. Holt, The beta to alpha phase transformation in zircaloy-4, Journal of Nuclear Materials. 35 (1970) 322–334. doi:10.1016/0022-3115(70)90216-3.

27 O.T. Woo, K. Tangri, Transformation characteristics of rapidly heated and quenched zircaloy-4-oxygen alloys, Journal of Nuclear Materials. 79 (1979) 83–94.

28 Kenneth Easterling, Chapter3 - The heat-affected zone, In Introduction to the Physical Metallurgy of Welding (Second Edition), Butterworth-Heinemann, 1992, Pages 126-190

29 T. Forgeron, J. C. Brachet, F. Barcelo, A. Castaing, J. Hivroz, J. P. Mardon, and C. Bernaudat. Experiment and modeling of advanced fuel rod cladding under LOCA conditions: alpha-beta phase kinetics and EDGAR methodology. In G. P. Sabol and G. D. Moan, editors, Zirconium in Nuclear Industry: Twelfth International Symposium, volume ASTM STP 1345, pages 256–278, West Conshohocken, PA, USA, 2000. American Society for Testing and Materials.

30 A.R. Massih, T. Andersson, P. Witt, M. Dahlbäck, M. Limbäck, Effect of quenching rate on the β-to-α phase transformation structure in zirconium alloy, Journal of Nuclear Materials. 322 (2003) 138–151. doi:10.1016/S0022-3115(03)00323-4.

---

31 E. Tenckhoff, P.L. Rittenhouse, Annealing textures in zircaloy tubing, Journal of Nuclear Materials. 35 (1970) 14–23. doi:10.1016/0022-3115(70)90022-X.

32 R.A. Lebensohn, M.I. Gonzalez, Measurement and prediction of texture development during a rolling secuence of Zry-4 tubes, Journal of Nuclear Materials. (1996) 57–64.

33 K. Linga Murty, I. Charit, Texture development and anisotropic deformation of zircaloys, Progress in Nuclear Energy. 48 (2006) 325–359. doi:10.1016/j.pnucene.2005.09.011.

34 H.J. Bunge and C.U. Nauer-Gerhardt: Titanium Science and Technology, DGM, Frankfurt, Germany, 1985, vol. 3, p. 1713.

35 N. Bozzolo, N. Dewobroto, T. Grosdidier, F. Wagner, Texture evolution during grain growth in recrystallized commercially pure titanium, Materials Science and Engineering: A. 397 (2005) 346–355. doi:10.1016/j.msea.2005.02.049.

36 K.Y. Zhu, B. Bacroix, T. Chauveau, D. Chaubet, O. Castelnau, Texture Evolution and Associated Nucleation and Growth Mechanisms during Annealing of a Zr Alloy, Metallurgical and Materials Transactions A. 40 (2009) 2423–2434. doi:10.1007/s11661-009-9909-y.

37 J.J. Kearns, Thermal expansion and preferred orientation in Zircaloy, WAPD TM-472, Westinghouse Electric Corp., Pittsburgh, PA, 1965.

38 D. Kerr, C. Cochrane, M.R. Daymond, “Phase Transformation and Variant Selection of Zr2.5Nb Pressure Tube”, submitted to Acta Mater.

39 PS Davies, BP Wynne, WM Rainforth, MJ Thomas, PL Threadgill, “Development of Microstructure and Crystallographic Texture during Stationary Shoulder Friction Stir Welding of Ti-6Al-4V”, Met. and Mat. Trans. A, v42A(8), p2278-2289, 2011.

40 C. Chauvy, P. Barberis, F. Montheillet, Microstructure transformation during warm working of β-treated lamellar Zircaloy-4 within the upper α-range, Materials Science and Engineering: A. 431 (2006) 59–67. doi:10.1016/j.msea.2006.05.031.

41 P. Barbéris, F. Montheillet, C. Chauvy, Variant Selection in Zr Alloys: How Many Variants Generated from one Beta Grain?, Solid State Phenomena. 105 (2005) 133–138. doi:10.4028/www.scientific.net/SSP.105.133.

42 L. Chai, B. Luan, M. Zhang, K.L. Murty, Q. Liu, Experimental observation of 12 α variants inherited from one β grain in a Zr alloy, Journal of Nuclear Materials. 440 (2013) 377–381. doi:10.1016/j.jnucmat.2013.05.053.

43 N. Gey, M. Humbert, M.J. Philippe, Y. Combres, Investigation of the α- and β- texture evolution of hot rolled Ti-64 products, Materials Science and Engineering: A. 219 (1996) 80–88. doi:10.1016/S0921-5093(96)10388-9.

44 D. Bhattacharyya, G. B. Viswanathan, H. L. Fraser, Crystallographic and morphological relationships between β phase and the Widmanstätten and allotriomorphic α phase at special β grain boundaries in an α/β titanium alloy, Acta Materialia 55.20 (2007): 6765-6778.